

This item is the archived peer-reviewed author-version of:

Simulating the onset of spring vegetation growth across the Northern Hemisphere

**Reference:**

Liu Qiang, Fu Yongshuo, Janssens Ivan, Piao Shilong, Liu Yongwen.- Simulating the onset of spring vegetation growth across the Northern Hemisphere  
Global change biology - ISSN 1354-1013 - 24:3(2018), p. 1342-1356  
Full text (Publisher's DOI): <https://doi.org/10.1111/GCB.13954>  
To cite this reference: <https://hdl.handle.net/10067/1496880151162165141>

1   **Title: Simulating the onset of spring vegetation growth across the Northern Hemisphere**

2   **Running head: simulating spring vegetation growth onset**

3

4                 Qiang Liu<sup>1</sup>, Yongshuo H. Fu<sup>1,2</sup>, Yongwen Liu<sup>1</sup>, Ivan A. Janssens<sup>2</sup>, Shilong Piao<sup>1\*</sup>

5

6                 <sup>1</sup> Sino-French Institute for Earth System Science, College of Urban and Environmental Sciences,  
7                 Peking University, Beijing 100871, China

8                 <sup>2</sup> Centre of Excellence PLECO (Plant and Vegetation Ecology), Department of Biology, University  
9                 of Antwerp, Universiteitsplein 1, B-2610 Wilrijk, Belgium

10

11   **Keywords:** Chilling, climate change, model evaluation, photoperiod, remote sensing, spring  
12                 phenology model

13

14                 Revised Manuscript for *Global Change Biology*

15

16   **\*Corresponding author:** Shilong Piao, Tel: +86 10 6275 3298, Email: slpiao@pku.edu.cn

17   **Paper type:** Primary Research Articles

18    **Abstract**

19    Changes in the spring onset of vegetation growth in response to climate change can profoundly  
20    impact climate–biosphere interactions. Thus, robust simulation of spring onset is essential to  
21    accurately predict ecosystem responses and feedback to ongoing climate change. To date, the  
22    ability of vegetation phenology models to reproduce spatiotemporal patterns of spring onset at  
23    larger scales has not been thoroughly investigated. In this study, we took advantage of phenology  
24    observations via remote sensing to calibrate and evaluated six models, including both one-phase  
25    (considering only forcing temperatures) and two-phase (involving forcing, chilling, and  
26    photoperiod) models across the Northern Hemisphere between 1982 and 2012. Overall, we found  
27    that the model that integrated the photoperiod effect performed best at capturing spatiotemporal  
28    patterns of spring phenology in boreal and temperate forests. By contrast, all of the models  
29    performed poorly in simulating the onset of growth in grasslands. These results suggest that the  
30    photoperiod plays a role in controlling the onset of growth in most Northern Hemisphere forests,  
31    whereas other environmental factors (e.g., precipitation) should be considered when simulating the  
32    onset of growth in grasslands. We also found that the one-phase model performed as well as the  
33    two-phase models in boreal forests, which implies that the chilling requirement is probably fulfilled  
34    across most of the boreal zone. Conversely, two-phase models performed better in temperate forests  
35    than the one-phase model, suggesting that photoperiod and chilling play important roles in these  
36    temperate forests. Our results highlight the significance of including chilling and photoperiod  
37    effects in models of the spring onset of forest growth at large scales, and indicate that the  
38    consideration of additional drivers may be required for grasslands.

39 **Introduction**

40 The timing of spring vegetation growth onset has significantly advanced due to global warming  
41 over the past decades, and this has substantially impacted interactions between the atmosphere and  
42 terrestrial ecosystems (Walther *et al.*, 2002; Menzel *et al.*, 2006; Piao *et al.*, 2007; Peñuelas &  
43 Filella, 2009; Friedl *et al.*, 2014; Piao *et al.*, 2017). Numerous phenology models, typically  
44 parameterized with ground-based phenological observations under ambient climatic conditions  
45 (Cannell & Smith, 1983; Hänninen, 1990; Kramer, 1994a; Chuine, 2000), have been developed and  
46 embedded into state-of-the-art land surface models (LSMs) to simulate the response and feedback  
47 of vegetation to climate change (Botta *et al.*, 2000; Sitch *et al.*, 2003; Krinner *et al.*, 2005).  
48 However, a recent study reported that current vegetation phenology models generate considerable  
49 uncertainties in these LSMs, consequently leading to large biases in the estimation of ecosystem  
50 carbon balances (Richardson *et al.*, 2012). Therefore, improved modeling of vegetation spring  
51 phenology at large scales is essential to reliably simulate the impact of climate change on  
52 vegetation growth and ecosystem carbon, water, and nutrient cycles.

53

54 Previous studies have reported the complex role of environmental cues in regulating the onset date  
55 of vegetation growth in spring. Temperature is generally considered as the main driver of spring  
56 onset (Cannell & Smith, 1983; Hänninen, 1990; Menzel *et al.*, 2006; Piao *et al.*, 2015), whereas  
57 photoperiod (Körner & Basler, 2010; Laube *et al.*, 2014a; Chuine *et al.*, 2016; Zohner *et al.*, 2016),  
58 air humidity (Laube *et al.*, 2014b), and precipitation (Forkel *et al.*, 2015; Fu *et al.*, 2014)  
59 co-determine vegetation growth onset dates for specific plant functional types and/or in specific  
60 regions. Based on these findings, various process-based models have been proposed to simulate the  
61 spring onset of growth. These models can be categorized into two types. One-phase models (e.g.,

62 the Spring Warming model) only involve the ecodormancy phase, and consider the day when  
63 accumulated forcing temperatures reach a required threshold (i.e., the heat requirement) to be the  
64 date of leaf unfolding (Sarvas, 1974). Two-phase models, such as the Sequential, Parallel, Unified,  
65 UniChill, and DORMPHOT models (Hänninen, 1990; Kramer, 1994b; Chuine, 2000; Caffarra *et al.*,  
66 2011a), involve both the endodormancy and ecodormancy phases. These models assume that a  
67 certain amount of chilling is required to break endodormancy, and that a certain amount of heat  
68 must be accumulated to break ecodormancy and induce leaf unfolding (Cannell & Smith, 1983;  
69 Murray *et al.*, 1989; Myking & Heide, 1995). The DORMPHOT model also integrates the  
70 photoperiod effect and assumes that increased photoperiod (longer days) promotes the rate of  
71 forcing accumulation during the ecodormancy phase (Caffarra *et al.*, 2011a). Overall, one-phase  
72 and two-phase models differ in their assumptions regarding the control over spring phenology  
73 processes, and consequently predict widely diverging spring growth onset dates under future,  
74 warmer conditions.

75

76 Phenology models have generally been calibrated using ground-based records for specific plant  
77 species, and have provided reasonable simulations of local conditions and similar climatic regions  
78 (Hunter & Lechowicz, 1992; Chuine, 2000; Migliavacca *et al.*, 2011; Jeong *et al.*, 2013; Melaas *et*  
79 *al.*, 2013a). However, these locally parameterized models cannot simply be extrapolated to larger  
80 scales (Cleland *et al.*, 2007; Rayner, 2010). In contrast to ground-based phenology observations,  
81 remotely sensed satellite imagery provides spring phenology estimates at the landscape scale  
82 (White *et al.*, 2009; Jeong *et al.*, 2011; Wang *et al.*, 2015), bridging plant physiology and ecosystem  
83 processes as they relate to global change (Díaz & Cabido, 1997) at the same resolution as  
84 state-of-the-art LSMs. Therefore, satellite-based phenological observations are ideal for optimizing

85 phenology models (Peñuelas & Filella, 2009) and for scaling up site-level phenological models to  
86 regional and even global scales. Several studies have investigated vegetation phenology models at  
87 the regional scale using satellite-derived estimates of the starting date of the growing season (SOS)  
88 (Yang *et al.*, 2012; Melaas *et al.*, 2015; Xin *et al.*, 2015; Chen *et al.*, 2016); however, these studies  
89 only considered forcing and/or chilling, ignoring the effects of photoperiod, whose role is expected  
90 to become increasingly important under future climate warming conditions (Fu *et al.*, 2015).

91

92 In the current study, we calibrated and evaluated six widely used spring phenology models,  
93 including one-phase and two-phase chilling and photoperiod models, using remote-sensing based  
94 SOS inferred from a newly released GIMMS (Global Inventory Modelling and Mapping Studies)  
95 NDVI (Normalized Difference Vegetation Index) dataset from 1982 to 2012. The primary goals of  
96 this study were (1) to calibrate different vegetation spring phenology models across the Northern  
97 Hemisphere; (2) to evaluate and identify an optimal model for specific plant functional types (PFTs)  
98 in reproducing spatiotemporal SOS patterns; and (3) to explore the chilling, forcing, and  
99 photoperiod effects in modeling vegetation growth onset for each PFT.

100 **Materials and Methods**

101 *Datasets*

102 *Climate data and vegetation map.* Daily temperature data with a spatial resolution of  $0.5^\circ \times 0.5^\circ$  was  
103 retrieved from the CRU-NCEP v5 climate dataset (available at  
104 [ftp://nacp.ornl.gov/synthesis/2009/frescati/model\\_driver/cru\\_ncep/analysis/readme.htm](ftp://nacp.ornl.gov/synthesis/2009/frescati/model_driver/cru_ncep/analysis/readme.htm)), spanning  
105 the study period from 1982 to 2012. This dataset was generated from NCEP reanalysis and  
106 CRU-TS climatology data (New *et al.*, 2000; Mitchell & Jones, 2005). Vegetation type data used in  
107 this study was adapted from a land cover dataset based on PFT (Verant *et al.*, 2004; MacBean *et al.*,  
108 2015). We focused on natural vegetation across the Northern Hemisphere (latitudes exceeding  $30^\circ$   
109 N) including three temperate forests, two boreal forests, and two grasslands. We did not take  
110 regions dominated by cropland into consideration, because cropland did not exhibit clear  
111 seasonality and was more susceptible to interruption by human activities. To eliminate the effects of  
112 any spatial mismatch between the two datasets, we remapped the PFT map into the same spatial  
113 resolution as the temperature data and calculated the fraction of PFT located within each  $0.5^\circ \times 0.5^\circ$   
114 pixel. Finally, seven PFTs were chosen, including temperate needleleaf evergreen (TeNE), temperate  
115 broadleaved evergreen (TeBE), temperate broadleaved deciduous (TeBD), boreal needleleaf  
116 evergreen (BoNE), boreal broadleaved deciduous (BoND), natural C3 grass (NC3), and natural C4  
117 grass (NC4) (Fig. S1).

118

119 *Satellite-derived phenology.* The seasonal cycle of NDVI serves as a proxy for vegetation greenness  
120 and photosynthetic activity (Myneni & Hall, 1995; Myneni *et al.*, 1997), and is thus widely applied  
121 in the extraction of vegetation phenology at the regional and global scales (Buitenwerf *et al.*, 2015;  
122 Garonna *et al.*, 2015; Piao *et al.*, 2015). In this study, we estimated the satellite-derived SOS from

123 the latest release of the GIMMS NDVI datasets ( $\text{NDVI}_{3g.v1}$ ) at a spatial resolution of  $1/12^\circ \times 1/12^\circ$   
124 during the period from 1982 to 2012. Apart from the update of satellite sensors, atmospheric  
125 interference, and non-vegetation dynamics addressed in  $\text{NDVI}_{3g}$  (Pinzon & Tucker, 2014), artifacts  
126 associated with snow coverage and changes in calibration that took place after 2006 were processed  
127 (Pinzon & Tucker, 2016). Following the methods of previous studies (Jakubauskas *et al.*, 2001;  
128 Zhang *et al.*, 2003; Piao *et al.*, 2006; Julien & Sobrino, 2009), we estimated SOS using four  
129 commonly used phenology extraction methods (i.e., Hants-Mr, Polyfit-Mr, double logistic, and  
130 piecewise logistic), which depend on either predefined thresholds or changing characteristics of the  
131 NDVI curve (Liu *et al.*, 2016). To reduce the uncertainty resulting from different interpretations of  
132 SOS from NDVI data, we applied an average SOS value derived from the four methods in the  
133 following analysis. As with the resample of the PFT map, we categorized all of the SOS data  
134 located in  $0.5^\circ \times 0.5^\circ$  pixels into specific PFTs, and then calculated the average for each PFT in each  
135 pixel.

136

#### 137 *Spring phenology models*

138 Six spring phenology models, including the one-phase Spring Warming model and two-phase  
139 Sequential, Parallel, Unified, UniChill, and DORMPHOT models, were employed in this study.  
140 These models were calibrated on a daily basis, using gridded SOS and temperature data. The  
141 modeled SOS was defined as the day when the state of forcing ( $S_f$ ) reached its critical value ( $F_{\text{crit}}$ ). A  
142 detailed description of these models is provided below.

143

144 *Spring Warming model.* The one-phase spring warming model only considers the influence of  
145 forcing and calculates the accumulated daily rate of forcing ( $R_f$ ) according to a logistic function (Eq.

146 1) (Sarvas, 1974) starting from  $t_0$  (set as January 1 of the current year). Therefore, the SOS date is  
 147 defined as the date when  $S_f$  exceeds  $F_{crit}$ :

$$148 \quad S_f = \sum_{t_0}^t R_f = \sum_{t_0}^t \frac{A_f}{1 + e^{\alpha(T - \beta)}} \quad (1)$$

149

150 *Sequential model.* The Sequential model assumes that the accumulation of forcing will not start  
 151 until a critical threshold ( $C_{crit}$ ) of chilling state ( $S_c$ , a daily sum of chilling rates) is met (Kramer,  
 152 1994b). In this model, the rate of chilling ( $R_c$ ) is described using a triangular function (Hänninen,  
 153 1990) (Eq. 2) and  $S_c$  begins to accumulate after September 1 of the previous year, according to the  
 154 methods of previous studies (Eq. 3) using a 1-day time step (Chuine, 2000). This model uses an  $R_f$   
 155 similar to that of the Spring Warming model, but with a competence function ( $K$ ) (Eqs. 4 and 5).  
 156 The forcing begins to accumulate when the daily temperature ( $T$ ) is greater than  $T_d$  and  $C_{crit}$  is  
 157 fulfilled:

$$158 \quad R_c = \begin{cases} 0, & T \leq T_a \\ \frac{T - T_a}{T_b - T_a}, & T_a < T \leq T_b \\ \frac{T - T_c}{T_b - T_c}, & T_b < T < T_c \\ 0, & T \geq T_c \end{cases} \quad (2)$$

$$159 \quad S_c = \sum_{t_c}^t R_c \quad (3)$$

$$160 \quad K = \begin{cases} 1, & S_c \geq C_{crit} \\ 0, & S_c < C_{crit} \end{cases} \quad (4)$$

$$161 \quad R_f = \begin{cases} 0, & T \leq T_d \\ K \frac{Af}{1 + e^{\alpha(T + \beta)}}, & T > T_d \end{cases} \quad (5)$$

$$162 \quad S_f = \sum_{t_c}^t R_f \quad (6).$$

163

164    *Parallel model.* Unlike the Sequential model, the Parallel model assumes that forcing functions  
 165    even when  $C_{crit}$  has not been attained (Landsberg, 1974); however, the parameters  $R_c$ ,  $S_c$ , and  $R_f$  are  
 166    exactly the same as in the Sequential model. The competence function ( $K$ , Eq. 7), however,  
 167    introduces another parameter ( $K_{min}$ ), determining the minimum potential of an unchilled bud to  
 168    respond to the forcing temperature (Hänninen, 1990; Kramer, 1994b). Therefore, the state of  
 169    chilling and forcing could increase simultaneously over time:

$$170 \quad K = \begin{cases} K_{min} + \frac{1 - K_{min}}{C_{crit}} S_c, & S_c < C_{crit} \\ 1, & S_c \geq C_{crit} \end{cases} \quad (7).$$

171

172    *Unified model.* The Unified model (Chuine, 2000) applies paired sigmoid functions to describe  $R_c$   
 173    and  $R_f$ . The accumulation of chilling ( $S_c$ , Eq. 8) starts at  $t_c$  (fixed on September 1 of the previous  
 174    year) and continues even after  $C_{crit}$  is attained. Forcing begins after the chilling critical state, and  
 175    the forcing requirement for leaf-out (i.e., the critical state of forcing,  $F_{crit}$ ), is an experimental  
 176    function of the total chilling accumulation ( $C_{tot}$ ) (Eq. 11):

$$177 \quad S_c = \sum_{t_c}^t R_c = \sum_{t_c}^t \frac{1}{1 + e^{T_a(T-T_c)^2 + T_b(T-T_c)}} \quad (8)$$

$$178 \quad C_{tot} = \sum_{t_c}^{t_c + deltaP} R_c = \sum_{t_c}^{t_c + deltaP} \frac{1}{1 + e^{T_a(T-T_c)^2 + T_b(T-T_c)}} \quad (9)$$

$$179 \quad S_f = \sum_{t_0}^t R_f = \sum_{t_0}^t \frac{1}{1 + e^{\alpha(T-T_d)}} \quad (10)$$

$$180 \quad F_{crit} = w e^{z C_{tot}} \quad (11).$$

181

182    *UniChill model.* The Unichill model is simplified from the Unified model (Chuine, 2000), and is

183 similar to the Sequential model. The difference between the UniChill and Sequential models is the  
 184 rate function incorporating chilling and forcing accumulation. The UniChill model uses the same  $R_c$   
 185 and  $R_f$  as the Unified model. The accumulation of chilling begins September 1 of the previous year  
 186 (Eq. 12), and continues until  $C_{crit}$  is reached. Forcing ( $S_f$ ) begins once  $C_{crit}$  is attained (Eq. 13) and  
 187 leaf-out begins when  $F_{crit}$  is reached (i.e., SOS):

$$188 \quad S_c = \sum_{t_c}^t R_c = \sum_{t_c}^t \frac{1}{1 + e^{T_a(T-T_c)^2 + T_b(T-T_c)}} \quad (12)$$

$$189 \quad S_f = \sum_{t_l}^t R_f = \sum_{t_l}^t \frac{1}{1 + e^{\alpha(T-\beta)}} \quad (13).$$

190

191 *DORMPHOT model.* The DORMPHOT model integrates the photoperiod effect to improve the  
 192 simulation of budburst (Caffarra *et al.*, 2011a), which involves dormancy induction, dormancy  
 193 release, and growth resumption. In this model, dormancy induction is triggered by both short  
 194 photoperiods ( $DR_p$ ) and low temperatures ( $DR_t$ ), and is complete when the state of dormancy  
 195 induction ( $DS$ , Eq. 14) reaches a critical value ( $D_{crit}$ ):

$$196 \quad DS = \sum_{t_0}^t DR_T \times DR_p = \sum_{t_0}^t \frac{1}{1 + e^{aD(T-bD)}} \times \frac{1}{1 + e^{10(DL-DL_{crit})}} \quad (14),$$

197 where  $t_0$  is the start date of dormancy induction (fixed to September 1 of the year preceding  
 198 budburst),  $T$  is the daily mean temperature, and  $DL$  is day length on day  $t$ . Dormancy release and  
 199 growth resumption then begin. As in the Unified model,  $S_c$  is defined as the daily sum of  $R_c$  after  $t_d$   
 200 (the day when dormancy induction is complete) as follows:

$$201 \quad S_c = \sum_{t_d}^t R_c = \sum_{t_d}^t \frac{1}{1 + e^{aC(T-cC)^2 + (T-cC)}} \quad (15).$$

202 By contrast,  $R_f$  is determined by both photoperiod and  $S_c$ . Long days above a certain threshold  
 203 increases  $R_f$  (i.e., photoperiod sensitivity), which is in turn promoted by a longer previous chilling

204 exposure or accumulation by decreasing this threshold (Caffarra *et al.*, 2011b). This mechanism is  
 205 characterized by Equations 16–18. The mid-response temperature ( $T_{50}$ ) decreases as DL increases,  
 206 and results in an increase in  $R_f$  (Eq. 16).  $DL_{50}$  corresponds to the critical day length at which  $T_{50}$  is  
 207 30°C and decreases with higher  $S_c$  (Eqs. 17–18). This negative relationship is set by parameters  $gT$  ( $\geq$   
 208 0) and  $hDL$  ( $\geq 0$ ), respectively.

$$209 \quad S_f = \sum_{t_d}^t R_f = \sum_{t_d}^t \frac{1}{1 + e^{dF(T - T_{50})}} \quad (16)$$

$$210 \quad T_{50} = \frac{60}{1 + e^{gT(DL - DL_{50})}} \quad (17)$$

$$211 \quad DL_{50} = \frac{24}{1 + e^{hDL(S_c - C_{crit})}} \quad (18).$$

212

### 213 *Model calibrations using satellite-derived SOS*

214 The minimum root mean square error (RMSE, Eq. 19) was used as the criterion to calibrate the  
 215 parameters of the models given in Table 1. Bayesian optimization techniques (Mockus, 2012;  
 216 Martinez-Cantin, 2014) were applied to determine the minimum RMSE and the corresponding  
 217 parameter set for each PFT. The model parameters were constrained within a range based on the  
 218 literature, and a Gaussian process model of the objective function (i.e., RMSE between model  
 219 simulations and satellite observations) was maintained to train the model. Then the next point to  
 220 evaluate was determined by an acquisition function, which could balance sampling at points with  
 221 low-modeled objective functions and help to find an optimal boundary value. To evaluate the  
 222 robustness of these models, PFT-specific samples for model internal (90%) and external (10%)  
 223 validation were randomly sampled from satellite-derived SOS. In addition to RMSE, other metrics  
 224 were introduced to assess model performance for specific PFT. For example, the Akaike  
 225 Information Criterion (AIC, see Eq. 20) trades off the goodness of fit and the complexity of the

226 models, with lower AIC values indicating better model simulation (Akaike, 1998). Following Chen  
 227 (2017), the Nash–Sutcliffe Efficiency index (NSE, Eq. 21) (Nash & Sutcliffe, 1970) was applied to  
 228 quantitatively describe the reliability of the calibrated models. Positive NSE (varies from 0 to 1,  
 229 higher = better) indicates that the model explained more variance than the null model (i.e., mean  
 230 SOS):

$$231 \quad RMSE = \sqrt{\frac{\sum_{i=1}^n (obs_i - pre_i)^2}{n}} \quad (19)$$

$$232 \quad AIC = n \times \ln \left( \frac{\sum_{i=1}^n (obs_i - pre_i)^2}{n} \right) + 2(k+1) \quad (20)$$

$$233 \quad NSE = 1 - \frac{\sum_{i=1}^n (obs_i - pre_i)^2}{\sum_{i=1}^n (obs_i - \overline{obs})^2} \quad (21),$$

234 where  $obs_i$  and  $pre_i$  are pixel–year observed and predicted SOS, respectively;  $\overline{obs}$  is the mean  
 235 value of observed SOS;  $n$  is the number of pixel–year SOS;  $k$  is the number of parameters in each  
 236 model.

237 **Results**

238 *Best model for each PFT*

239 Table 1 summarizes the optimal parameters for each of the six models for each PFT, as well as the  
240 internal and external model evaluations. Overall, the models performed better than the null model  
241 (mean SOS) across all of the PFTs (i.e., NSE > 0). The percentage of variance explained by the  
242 models ranged from 24% (NC4, Parallel model) to 82% (NC3, DORMPHOT model), and varied  
243 greatly among the PFTs and models. Models generally performed better for the boreal forest than  
244 the temperate forest (Table 1, Figs. 1 and S2). For the boreal forest, although the one-phase spring  
245 warming model performed similarly to the two-phase models, the UniChill and DORMPHOT  
246 models performed slightly better in BoND (RMSE: approximately 9 days) and BoNE (RMSE:  
247 approximately 12 days) than the other models, according to the lowest AIC values (Table 1). In  
248 temperate forests, the two-phase models generally outperformed the one-phase model. The  
249 DORMPHOT model performed best for TeNE, TeBE, and TeBD (RMSE: approximately 14 days)  
250 (Table 1, Figs. 1 and S2). In the two grassland ecosystems, these models could not successfully  
251 reproduce the SOS dates, particularly in NC4, because the RMSE was greater than 21 days (Table 1,  
252 Figs. 1 and S2).

253

254 *Evaluation of spring phenology models at the regional scale*

255 The spatial patterns of SOS predicted by the six calibrated models during the period 1982–2012  
256 were broadly similar to those of the satellite-derived SOS, with spatial correlation coefficients  
257 ranging from 0.91 to 0.94 (Fig. 2). Nonetheless, model predictions differed greatly from satellite  
258 observations in western America and in arid/semi-arid regions (e.g., central Eurasia, Fig. 2).  
259 Moreover, SOS generally occurred earlier in low latitudes but later in the middle and higher

260 latitudes (Fig. 2a). We found that such latitude gradients in satellite-derived SOS were captured  
261 precisely by model simulations except by the Parallel and Unichill models, which showed slight  
262 disagreement in latitudes lower than 35°N (Fig. 2e and i). Within boreal forests, all six models were  
263 in quite close agreement, with less than 10 days of difference in long-term mean SOS in more than  
264 68% of BoNE and 85% of BoND (Fig. S3). In temperate forests, the spring warming model  
265 displayed the largest differences, whereas the DORMPHOT model agreed best with the satellite  
266 observations (Fig. S3). The largest discrepancies between model predictions and observations were  
267 found in the C4 grasslands (Fig. S3). Across the Northern Hemisphere, all of the six models  
268 predicted SOS with a median RMSE of 7–15 days for forests and 10–18 days for grasslands (Fig.  
269 3). Within forests, boreal forest (e.g., BoNE and BoND) generally exhibited the highest overall  
270 accuracy (with a median RMSE of < 10 days), whereas within grasslands, the spring phenology of  
271 C4 grasses was very poorly captured by the models (Fig. 3). In temperate forests, the one-phase  
272 Spring Warming model displayed poorer accuracy than the two-phase models involving chilling  
273 and photoperiod effects (mainly for TeNE and TeBE, Fig. 3a). The spatial distribution of RMSE  
274 indicated better agreement with satellite observations at latitudes higher than 45°N (e.g., RMSE <  
275 10 days, except for the one-phase spring warming model), whereas higher RMSE values (e.g., > 15  
276 days) were obtained in lower latitudes, such as western America and central Eurasia (Figs. 4 and  
277 S4). Across the Northern Hemisphere (Fig. 4g), the two-phase DORMPHOT, Unified, and  
278 Sequential models showed the best accuracy (with median RMSE = 9.3, 9.5, 9.8 days, respectively),  
279 and the poorest performance was found in the one-phase Spring Warming model (median RMSE =  
280 11.9 days).

281

282    *Evaluation of predicted SOS trends in the past three decades*

283    During the period of 1982–2012, the modeled advancing trends in SOS in the Northern Hemisphere  
284    were obtained by the six models, which were in good agreement with the observations (Fig. 5). The  
285    model predictions captured SOS trends across approximately 74% (Parallel) to 78% (DORMPHOT)  
286    of the study area, although their magnitudes were weaker than the observations (Fig. 5). The  
287    differences in trends between satellite-derived SOS and model predictions were mainly distributed  
288    in northeastern Europe and southwestern North America (Fig. 5), which are primarily covered by  
289    TeBE and grasslands (Fig. S5). At the PFT scale, satellite observations documented a significant  
290    trend towards earlier SOS across all of the PFTs (except for NC4,  $P = 0.67$ ) during the period of  
291    1982–2012; however, the one-phase Spring Warming model generated non-significant changes in  
292    SOS, particularly in temperate forests, and the two-phase models showed good agreement with  
293    satellite observations in boreal, but not temperate, forest. Overall, the DORMPHOT model  
294    provided a better performance in trend simulations across most PFTs (Figs. 5, S5, and 6).

295

296 **Discussion**

297 Our study, covering a large spatial and temporal scale, revealed an overall median RMSE of 7–15  
298 days for forests and 10–18 days for grasslands between the model predictions and satellite-derived  
299 SOS (Fig. 3). The overall accuracy of the simulations was comparable with previous efforts limited  
300 to either fewer PFTs or much shorter study periods. For example, the models fitted for TeBD  
301 showed similar accuracy to those of Melaas *et al.* (2015) for the eastern United States (median  
302 RMSE: 5–10 days), although in our study, model predictions for TeBD in southern Europe showed  
303 larger differences with satellite-derived SOS (Figs. 4 and S4). The models reproduced SOS less  
304 accurately for grasslands than for forests in this study (e.g., NC4 in central America, NC3 in  
305 western America) and in previous research (Xin *et al.*, 2015), suggesting that other environmental  
306 factors besides spring forcing temperatures, chilling, and photoperiod should be considered in the  
307 phenology models. These factors may include soil moisture or precipitation, particularly in arid and  
308 semi-arid regions (Schwartz *et al.*, 2006; Forkel *et al.*, 2015). In terms of model-predicted SOS  
309 trends during the period of 1982–2012, advanced SOS trends were well captured among most PFTs  
310 (except for TeBE), with consistent signs but weaker magnitudes. These results may be related to the  
311 fact that current phenology models do not predict phenology dates well under extreme climate  
312 conditions, and that a few years' poor model predictions during the study period (e.g. 1983–1984,  
313 2005–2006 for TeBE and 1982–1983 for TeBD for most models) can result in a large bias in the  
314 trend estimation (Figure S6). Moreover, we found that this issue was less likely related to the model  
315 calibration, because the ensemble means of four phenology-extraction methods did not reduce the  
316 temporal variation as shown in the SOS at PFT scale using individual method (Figure S7).

317

318 Previous studies parameterized spring phenology models with ground phenological records and then

319 extended the ground-based models to regional and hemispherical scale (Schwartz *et al.*, 2006; Jeong  
320 *et al.*, 2013; Yang *et al.*, 2012). However, large unclear in understanding the mechanisms underlying  
321 leaf-out process, especially scaling them from species level to ecosystem level, is still existed and  
322 needs to be explored. In this study, we found that the Spring Warming model, which only involves  
323 thermal forcing, performed as well as two-phase models in the boreal forests (particularly for  
324 BoND), which is consistent with previous phenological modeling studies (Hunter & Lechowicz,  
325 1992; Vitasse *et al.*, 2011). This may be because the boreal forests experience long and cold winters,  
326 with chilling requirements largely satisfied even under the ongoing climate warming conditions  
327 (Chuine, 2000; Vitasse *et al.*, 2011; Xu & Chen, 2013). For temperate forests, however, a lower  
328 accuracy in predicting SOS was found in the Spring Warming model than in the two-phase models,  
329 implying that chilling is generally insufficient, and thus that chilling is an important factor in  
330 modeling spring phenology in temperate forests. This finding is also consistent with those of  
331 previous studies in temperate regions (Chuine *et al.*, 2010; Fu *et al.*, 2015). Importantly, we found  
332 that the DORMPHOT model, which incorporated the photoperiod effect, performed better in  
333 temperate deciduous and evergreen broadleaf forests, but yielded similar results in boreal or  
334 temperate evergreen needle-leaf forests. This finding is also supported by recent experimental  
335 studies that documented the fundamental but species-specific role of photoperiod in temperate tree  
336 species (Körner & Basler, 2010; Caffarra *et al.*, 2011b; Zohner *et al.*, 2016). Therefore, we  
337 conclude that the spring phenology of temperate forests might rely more on chilling and  
338 photoperiodic cues than boreal forest, which mainly depends on spring forcing temperatures under  
339 current climate conditions. With continued climate warming, however, chilling requirements might  
340 not be completely fulfilled in boreal forests, such that chilling and/or photoperiod might become  
341 more important in the spring onset process of these forests, although this speculation remains to be

342 tested experimentally.

343

344 Forecasts of spring vegetation growth onset and its variation under climate change scenarios  
345 depend largely on model structure, thereby requiring a better understanding of the interactions with  
346 environmental cues across different PFTs (Richardson *et al.*, 2012). In this study, models  
347 integrating chilling and photoperiod generally produced better agreement in spatiotemporal patterns  
348 with satellite-derived SOS, although their RMSEs remained high. This result illuminates the  
349 potential to further improve current temperature-driven models by considering more environmental  
350 and physiological factors. Previous studies based on either *in situ* or satellite observations reported  
351 statistically significant correlations between spring growth onset and other environmental cues,  
352 such as soil water content or precipitation (Peñuelas *et al.*, 2004; Bernal *et al.*, 2011; Fu *et al.*,  
353 2014), snowfall (Chen *et al.*, 2015), daytime (rather than daily mean) temperature (Piao *et al.*, 2015;  
354 Fu *et al.*, 2016) and successional status (Jeong *et al.*, 2013). Undoubtedly, these cues co-determine  
355 vegetation spring phenology; however, the mechanisms via which they influence the leaf-out  
356 process remain unclear. Further investigation through manipulative experiments at species and  
357 ecosystem level is necessary to make the models more biologically realistic, thus enhancing their  
358 predictive ability. Another possible source of uncertainty between satellite-derived SOS and model  
359 predictions may stem from the coarse spatial resolution of the observations applied in this analysis.  
360 The inclusion of different plant species within a pixel or specific PFT could misrepresent the  
361 response of spring onset to climate change (Chuine *et al.*, 2000; Fu *et al.*, 2014; MacBean *et al.*,  
362 2015), and recent studies have found substantial differences in chilling requirements and  
363 photoperiod sensitivities of different tree species (Körner & Basler, 2010; Laube *et al.*, 2014;  
364 Zohner *et al.*, 2016). Regional climate datasets and satellite-based spring phenology dates with

365 finer spatial resolution, as phenology data inferred from Landsat imagery (Melaas *et al.*, 2013b) are  
366 becoming increasingly available, and thus would be profitable for modeling spring phenology.  
367 Besides, the parameterization of spring phenology models might be the third source of uncertainties  
368 in simulating SOS. We applied the optimal parameters in models, while large spatial variation of  
369 model parameters may exist and the Markov Chain Monte Carlo (MCMC) approach may be a good  
370 reference when applying these models within the PFTs (Jeong *et al.*, 2012).

371

372 In conclusion, we calibrated six frequently applied spring phenology models using satellite-derived  
373 SOS, and compared their simulations across PFTs in the Northern Hemisphere during the period of  
374 1982–2012. Model performance relied strongly on their interpretations of the effects of forcing,  
375 chilling, and photoperiod. Across the Northern Hemisphere, forcing temperatures might play a  
376 prominent role in modeling boreal forest SOS (particularly for BoND), with the one-phase Spring  
377 Warming model (which considers only forcing temperature) showing similar accuracy to the  
378 two-phase models. By contrast, for temperate PFTs (e.g., TeNE and TeBE), models involving  
379 chilling and particularly photoperiod provided better simulations. Specifically, the DORMPHOT  
380 model (which represented the photoperiod effect) best captured the spatiotemporal pattern of SOS  
381 in most PFTs (except in TeBD). Our results suggest that chilling and photoperiod effects should be  
382 embedded in large-scale vegetation phenology simulations, albeit in a PFT-specific manner. Several  
383 issues, however, still need to be addressed: 1) incorporating soil moisture or precipitation in  
384 arid/semi-arid regions and snowmelt in higher altitudes to improve simulations in grasslands; and 2)  
385 applying climatic and phenology observational datasets with finer spatial and temporal resolutions.  
386 Moreover, manipulative experiments aimed toward elucidating environmental and biological  
387 mechanisms underlying spring vegetation growth onset are required to better predict the date of

388 SOS, and thus ecosystem responses to ongoing climate change.

389

390 **Acknowledgements**

391 This study was supported by the National Key R&D Program of China (2017YFA0604702), National  
392 Natural Science Foundation of China (41530528 and 31770516), the BELSPO STEREO project  
393 ECOPROPHET (SR00334) and National Youth Top-notch Talent Support Program in China. Y.S.H  
394 acknowledge support by the National Key Research and Development Program of China  
395 (2017YFA06036001).

396 **References**

- 397 Akaike, H. (1998) Information theory and an extension of the maximum likelihood principle. In:  
398       *Selected Papers of Hirotugu Akaike.* pp 199-213. Springer.
- 399 Bernal, M., Estiarte, M., & Peñuelas, J. (2011) Drought advances spring growth phenology of the  
400       Mediterranean shrub *Erica multiflora*. *Plant Biology*, 13, 252-257.
- 401 Botta, A., Viovy, N., Ciais, P., Friedlingstein, P., & Monfray, P. (2000) A global prognostic scheme  
402       of leaf onset using satellite data. *Global Change Biology*, 6, 709-725.
- 403 Buitenwerf, R., Rose, L., & Higgins, S.I. (2015) Three decades of multi-dimensional change in  
404       global leaf phenology. *Nature Climate Change*, 5, 364-368.
- 405 Caffarra, A., Donnelly, A., & Chuine, I. (2011a) Modelling the timing of *Betula pubescens* budburst.  
406       II. Integrating complex effects of photoperiod into process-based models. *Climate Research*,  
407       46, 159-170.
- 408 Caffarra, A., Donnelly, A., Chuine, I., & Jones, M.B. (2011b) Modelling the timing of *Betula*  
409       *pubescens* budburst. I. Temperature and photoperiod: a conceptual model. *Climate Research*,  
410       46, 147-157.
- 411 Cannell, M., & Smith, R. (1983) Thermal time, chill days and prediction of budburst in *Picea*  
412       *sitchensis*. *Journal of Applied Ecology*, 20, 951-963.
- 413 Chen, M., Melaas, E.K., Gray, J.M., Friedl, M.A., & Richardson, AD (2016) A new  
414       seasonal-deciduous spring phenology submodel in the Community Land Model 4.5: impacts  
415       on carbon and water cycling under future climate scenarios. *Global Change Biology*, 22,  
416       3675-3688.
- 417 Chen, X., An, S., Inouye, D.W., & Schwartz, M.D. (2015) Temperature and snowfall trigger alpine  
418       vegetation green-up on the world's roof. *Global Change Biology*, 21, 3635-3646.

- 419 Chen, X. (2017) *Spatiotemporal Processes of Plant Phenology: Simulation and Prediction*, Berlin  
420 Heidelberg, Springer-Verlag Berlin Heidelberg.
- 421 Chen, X., Wang, L., & Inouye, D.W. (2017) Delayed response of spring phenology to global  
422 warming in subtropics and tropics. *Agricultural and Forest Meteorology*, 234, 222-235.
- 423 Chiang, J-M., & Brown, K.J. (2007) Improving the budburst phenology subroutine in the forest  
424 carbon model PnET. *Ecological Modelling*, 205, 515-526.
- 425 Chuine, I. (2000) A unified model for budburst of trees. *Journal of Theoretical Biology*, 207,  
426 337-347.
- 427 Chuine, I., Cambon, G., & Comtois, P. (2000) Scaling phenology from the local to the regional level:  
428 advances from species - specific phenological models. *Global Change Biology*, 6, 943-952.
- 429 Chuine, I., Morin, X., & Bugmann, H. (2010) Warming, Photoperiods, and Tree Phenology. *Science*,  
430 329, 277-278.
- 431 Chuine, I., Bonhomme, M., Legave, J.M., García De Cortázar - Atauri I, Charrier, G., ... Améglio, T.  
432 (2016) Can phenological models predict tree phenology accurately in the future? The  
433 unrevealed hurdle of endodormancy break. *Global Change Biology*, 22, 3444-3460.
- 434 Cleland, E.E., Chuine, I., Menzel, A., Mooney, H.A., & Schwartz, M.D. (2007) Shifting plant  
435 phenology in response to global change. *Trends in ecology & evolution*, 22, 357-365.
- 436 Díaz, S., & Cabido, M. (1997) Plant functional types and ecosystem function in relation to global  
437 change. *Journal of Vegetation Science*, 463-474.
- 438 Donnelly, A., Salamin, N., & Jones, M.B. (2006) Changes in tree phenology: an indicator of spring  
439 warming in Ireland? In: *Biology and Environment: Proceedings of the Royal Irish Academy*.  
440 pp 49-56, JSTOR.
- 441 Forkel, M., Migliavacca, M., Thonicke, K., Reichstein, M., Schaphoff, S., ... Carvalhais, N. (2015)

- 442 Co-dominant water control on global inter-annual variability and trends in land surface  
443 phenology and greenness. *Global Change Biology*, 21, 3414-3435.
- 444 Friedl, M.A., Gray, J.M., Melaas, E.K., Richardson, AD., Hufkens, K., Keenan, T.F., . . . O'keefe, J.  
445 (2014) A tale of two springs: using recent climate anomalies to characterize the sensitivity of  
446 temperate forest phenology to climate change. *Environmental Research Letters*, 9, 054006.
- 447 Fu, Y.H., Piao, S., Op De Beeck, M., Cong, N., Zhao, H., Zhang, Y., . . . Janssens, I.A. (2014) Recent  
448 spring phenology shifts in western Central Europe based on multiscale observations. *Global  
449 Ecology and Biogeography*, 23, 1255-1263.
- 450 Fu, Y.H., Piao, S., Zhao, H., Jeong, S.J., Wang, X., Vitasse, Y., . . . Janssens, I.A. (2014) Unexpected  
451 role of winter precipitation in determining heat requirement for spring vegetation green-up at  
452 northern-middle and high latitudes. *Global Change Biology*, 20, 3743-3755.
- 453 Fu, Y.H., Piao, S., Vitasse, Y., Zhao, H., De Boeck, HJ., Liu, Q., . . . Janssens, I.A. (2015) Increased  
454 heat requirement for leaf flushing in temperate woody species over 1980-2012: effects of  
455 chilling, precipitation and insolation. *Global Change Biology*, 21, 2687–2697.
- 456 Fu, Y.H., Zhao, H., Piao, S., Peaucelle, M., Peng, S., Zhou, G., . . . Janssens, I.A. (2015) Declining  
457 global warming effects on the phenology of spring leaf unfolding. *Nature*, 526, 104-107.
- 458 Fu, Y.H., Liu, Y., De Boeck, HJ., Menzel, A., Nijs, I., Peaucelle, M., . . . Janssens, I.A. (2016) Three  
459 times greater weight of daytime than of night - time temperature on leaf unfolding phenology  
460 in temperate trees. *New Phytologist*, 212, 590-597.
- 461 Garonna, I., De Jong, R., & Schaepman, M. (2015) Variability and evolution of global land surface  
462 phenology over the past three decades (1982 - 2012). *Global Change Biology*, 22,  
463 1456-1468.
- 464 Hänninen, H. (1990) Modelling bud dormancy release in trees from cool and temperate regions. *Acta*

- 465 Forestalia Fennica, 213, 1-47.
- 466 Hunter, A.F., & Lechowicz, M.J. (1992) Predicting the Timing of Budburst in Temperate Trees.  
467 Journal of Applied Ecology, 29, 597-604.
- 468 Jakubauskas, M.E., Legates, D.R., & Kastens, J.H. (2001) Harmonic analysis of time-series AVHRR  
469 NDVI data. Photogrammetric Engineering and Remote Sensing, 67, 461-470.
- 470 Jeong, S.J., Ho, C.H., Gim, H.J., & Brown, M.E. (2011) Phenology shifts at start vs. end of growing  
471 season in temperate vegetation over the Northern Hemisphere for the period 1982–2008.  
472 Global Change Biology, 17, 2385-2399.
- 473 Jeong, S.J., Medvigy D, Shevliakova E, Malyshev S (2012) Uncertainties in terrestrial carbon  
474 budgets related to spring phenology. Journal of Geophysical Research: Biogeosciences, 117,  
475 G01030, doi:10.1029/2011JG001868.
- 476 Jeong, S.J., Medvigy, D., Shevliakova, E., & Malyshev, S. (2013) Predicting changes in temperate  
477 forest budburst using continental - scale observations and models. Geophysical Research  
478 Letters, 40, 359-364.
- 479 Julien, Y., & Sobrino, J. (2009) Global land surface phenology trends from GIMMS database.  
480 International Journal of Remote Sensing, 30, 3495-3513.
- 481 Körner, C., & Basler, D. (2010) Phenology under global warming. Science, 327, 1461-1462.
- 482 Kramer, K. (1994a) A modelling analysis of the effects of climatic warming on the probability of  
483 spring frost damage to tree species in The Netherlands and Germany. Plant, Cell &  
484 Environment, 17, 367-377.
- 485 Kramer, K. (1994b) Selecting a Model to Predict the Onset of Growth of *Fagus sylvatica*. Journal of  
486 Applied Ecology, 31, 172-181.
- 487 Krinner, G., Viovy, N., De Noblet - Ducoudré N, Ogée, J., Polcher, J., Friedlingstein, P., . . . Prentice,

- 488 I.C. (2005) A dynamic global vegetation model for studies of the coupled atmosphere -  
489 biosphere system. *Global Biogeochemical Cycles*, 19, doi: 10.1029/2003GB002199.
- 490 Landsberg, J. (1974) Apple fruit bud development and growth; analysis and an empirical model.  
491 *Annals of Botany*, 38, 1013-1023.
- 492 Laube, J., Sparks, T.H., Estrella, N., Hofler, J., Ankerst, D.P., & Menzel, A. (2014a) Chilling  
493 outweighs photoperiod in preventing precocious spring development. *Global Change  
494 Biology*, 20, 170-182.
- 495 Laube, J., Sparks, T.H., Estrella, N., & Menzel, A. (2014b) Does humidity trigger tree phenology?  
496 Proposal for an air humidity based framework for bud development in spring. *New  
497 Phytologist*, 202, 350-355.
- 498 Liu, Q., Fu, Y.H., Zhu, Z., Liu, Y., Liu, Z., Huang, M., . . . Piao, S. (2016) Delayed autumn phenology  
499 in the Northern Hemisphere is related to change in both climate and spring phenology. *Global  
500 Change Biology*, 22, 3702-3711.
- 501 Macbean, N., Maignan, F., Peylin, P., Bacour, C., Bréon, F.M., & Ciais, P. (2015) Using satellite data  
502 to improve the leaf phenology of a global terrestrial biosphere model. *Biogeosciences*, 12,  
503 7185-7208.
- 504 Martinez-Cantin, R. (2014) BayesOpt: a Bayesian optimization library for nonlinear optimization,  
505 experimental design and bandits. *Journal of Machine Learning Research*, 15, 3735-3739.
- 506 Melaas, E.K., Richardson, AD., Friedl, M.A., Dragoni, D., Gough, C.M., Herbst, M., . . . Moors, E.  
507 (2013a) Using FLUXNET data to improve models of springtime vegetation activity onset in  
508 forest ecosystems. *Agricultural and Forest Meteorology*, 171-172, 46-56.
- 509 Melaas, E.K., Friedl, M.A., & Zhu, Z. (2013b) Detecting interannual variation in deciduous  
510 broadleaf forest phenology using Landsat TM/ETM+ data. *Remote Sensing of Environment*,

- 511 132, 176-185.
- 512 Melaas, E.K., Friedl, M.A., & Richardson, AD. (2015) Multi-scale modeling of spring phenology  
513 across Deciduous Forests in the Eastern United States. *Global Change Biology*, 22, 792-805.
- 514 Menzel, A., Sparks, T.H., Estrella, N., Koch, E., Aasa, A., Ahas, R., . . . Briede, A. (2006) European  
515 phenological response to climate change matches the warming pattern. *Global Change  
516 Biology*, 12, 1969-1976.
- 517 Migliavacca, M., Galvagno, M., Cremonese, E., Rossini, M., Meroni, M., Sonnentag, O., . . . Busetto,  
518 L. (2011) Using digital repeat photography and eddy covariance data to model grassland  
519 phenology and photosynthetic CO<sub>2</sub> uptake. *Agricultural and Forest Meteorology*, 151,  
520 1325-1337.
- 521 Mitchell, T.D., & Jones, P.D. (2005) An improved method of constructing a database of monthly  
522 climate observations and associated high-resolution grids. *International Journal of  
523 Climatology*, 25, 693-712.
- 524 Mockus, J. (2012) *Bayesian approach to global optimization: theory and applications*, Springer  
525 Science & Business Media.
- 526 Murray, M., Cannell, M., & Smith, R. (1989) Date of budburst of fifteen tree species in Britain  
527 following climatic warming. *Journal of Applied Ecology*, 26, 693-700.
- 528 Myking, T., & Heide, O. (1995) Dormancy release and chilling requirement of buds of latitudinal  
529 ecotypes of *Betula pendula* and *B. pubescens*. *Tree physiology*, 15, 697-704.
- 530 Myneni, R.B., & Hall, F.G. (1995) The interpretation of spectral vegetation indexes. *Geoscience and  
531 Remote Sensing, IEEE Transactions on*, 33, 481-486.
- 532 Myneni, R.B., Keeling, C., Tucker, C., Asrar, G., & Nemani, R. (1997) Increased plant growth in the  
533 northern high latitudes from 1981 to 1991. *Nature*, 386, 698-702.

- 534 Nash, J.E., & Sutcliffe, J.V. (1970) River flow forecasting through conceptual models part I-A  
535 discussion of principles. *Journal of Hydrology*, 10, 282-290.
- 536 New, M., Hulme, M., & Jones, P. (2000) Representing twentieth-century space-time climate  
537 variability. Part II: Development of 1901-96 monthly grids of terrestrial surface climate.  
538 *Journal of Climate*, 13, 2217-2238.
- 539 Peñuelas, J., Filella, I., Zhang, X., Llorens, L., Ogaya, R., Lloret, F., . . . Terradas, J. (2004) Complex  
540 spatiotemporal phenological shifts as a response to rainfall changes. *New Phytologist*, 161,  
541 837-846.
- 542 Peñuelas, J., Filella, I. (2009) Phenology feedbacks on climate change. *Science*, 324, 887-888.
- 543 Piao, S., Fang, J., Zhou, L., Ciais, P., & Zhu, B. (2006) Variations in satellite-derived phenology in  
544 China's temperate vegetation. *Global Change Biology*, 12, 672-685.
- 545 Piao, S., Friedlingstein, P., Ciais, P., Viovy, N., & Demarty, J. (2007) Growing season extension and  
546 its impact on terrestrial carbon cycle in the Northern Hemisphere over the past 2 decades.  
547 *Global Biogeochemical Cycles*, 21, doi: 10.1029/2006GB002888.
- 548 Piao, S., Tan, J., Chen, A., Fu, Y.H., Ciais, P., Liu, Q., . . . Peñuelas, J. (2015) Leaf onset in the  
549 northern hemisphere triggered by daytime temperature. *Nature Communications*, 6,  
550 doi:10.1038/ncomms7911.
- 551 Piao, S.L., Liu, Z., Wang, T., Peng, S.S., Ciais, P., Huang, M.T., . . . Tans, P.P. (2017) Weakening  
552 temperature control on the interannual variations of spring carbon uptake across northern  
553 lands. *Nature Climate Change*, 7, 359-363
- 554 Pinzon, J.E., & Tucker, C.J. (2014) A non-stationary 1981–2012 AVHRR NDVI<sub>3g</sub> time series.  
555 *Remote Sensing*, 6, 6929-6960.
- 556 Pinzon, J.E., & Tucker, C.J. (2016) A Non-Stationary 1981-2015 AVHRR NDVI<sub>3g,v1</sub> Time Series: an

- 557 update. *Remote Sensing*, in preparation.
- 558 Richardson, AD., Black, T.A., Ciais, P., Delbart, N., Friedl, M.A., Gobron, N., . . . Luyssaert, S.  
559 (2010) Influence of spring and autumn phenological transitions on forest ecosystem  
560 productivity. *Philos Trans R Soc Lond B Biol Sci*, 365, 3227-3246.
- 561 Richardson, AD., Anderson, R.S., Arain, M.A., Barr, A.G., Bohrer, G., Chen, G., . . . Desai, A.R.  
562 (2012) Terrestrial biosphere models need better representation of vegetation phenology:  
563 results from the North American Carbon Program Site Synthesis. *Global Change Biology*, 18,  
564 566-584.
- 565 Sarvas, R. (1974) Investigations on the annual cycle of development of forest trees: II. Autumn  
566 dormancy and winter dormancy. *Communicationes Instituti Forestalis Fenniae*, 84, 101.
- 567 Schwartz, M.D., Ahas, R., & Aasa, A. (2006) Onset of spring starting earlier across the Northern  
568 Hemisphere. *Global Change Biology*, 12, 343-351.
- 569 Sitch, S., Smith, B., Prentice, I.C., Arneth, A., Bondeau, A., Cramer, W., . . . Sykes, M.T. (2003)  
570 Evaluation of ecosystem dynamics, plant geography and terrestrial carbon cycling in the LPJ  
571 dynamic global vegetation model. *Global Change Biology*, 9, 161-185.
- 572 Verant, S., Laval, K., Polcher, J., & De, Castro. M. (2004) Sensitivity of the continental hydrological  
573 cycle to the spatial resolution over the Iberian Peninsula. *Journal of Hydrometeorology*, 5,  
574 267-285.
- 575 Vitasse, Y., François, C., Delpierre, N., Dufrêne, E., Kremer, A., Chuine, I., & Delzon, S. (2011)  
576 Assessing the effects of climate change on the phenology of European temperate trees.  
577 *Agricultural and Forest Meteorology*, 151, 969-980.
- 578 Walther, G-R., Post, E., Convey, P., Menzel, A., Parmesan, C., Beebee, T.J., . . . Bairlein, F. (2002)  
579 Ecological responses to recent climate change. *Nature*, 416, 389-395.

- 580 Wang, X., Piao, S., Xu, X., Ciais, P., Macbean, N., Myneni, R.B., & Li, L. (2015) Has the advancing  
581 onset of spring vegetation green - up slowed down or changed abruptly over the last three  
582 decades? *Global Ecology and Biogeography*, 24, 621-631.
- 583 White, M.A., De Beurs, K.M., Didan, K., Inouye, D.W., Richardson, A.D., Jensen, O.P., . . .  
584 Lauenroth, W.K. (2009) Intercomparison, interpretation, and assessment of spring phenology  
585 in North America estimated from remote sensing for 1982–2006. *Global Change Biology*, 15,  
586 2335-2359.
- 587 Xin, Q., Broich, M., Zhu, P., & Gong, P. (2015) Modeling grassland spring onset across the Western  
588 United States using climate variables and MODIS-derived phenology metrics. *Remote  
589 Sensing of Environment*, 161, 63-77.
- 590 Xu, L., & Chen, X. (2013) Regional unified model - based leaf unfolding prediction from 1960 to  
591 2009 across northern China. *Global Change Biology*, 19, 1275-1284.
- 592 Yang, X., Mustard, J.F., Tang, J., & Xu, H. (2012) Regional - scale phenology modeling based on  
593 meteorological records and remote sensing observations. *Journal of Geophysical Research:*  
594 *Biogeosciences*, 117, doi: 10.1029/2012JG001977.
- 595 Zhang, X., Friedl, M.A., Schaaf, C.B., Strahler, A.H., Hodges, J.C., Gao, F., . . . Huete, A. (2003)  
596 Monitoring vegetation phenology using MODIS. *Remote Sensing of Environment*, 84,  
597 471-475.
- 598 Zohner, C.M., Benito, B.M., Svenning, J-C., & Renner, S.S. (2016) Day length unlikely to constrain  
599 climate-driven shifts in leaf-out times of northern woody plants. *Nature Climate Change*, 6,  
600 1120-1123.

601    **Supporting Information Captions**

602    **Figure S1.** Spatial distribution of the fractional cover of PFTs across the Northern Hemisphere ( $> 603$  30°N). Seven main PFTs were included: (a) Temperate needleleaf evergreen (TeNE), (b) Temperate  
604    broadleaved evergreen (TeBE), (c) Temperate broadleaved deciduous (TeBD), (d) Boreal needleleaf  
605    evergreen (BoNE), (e) Boreal needleleaf deciduous (BoND), (f) Natural C3 grass (NC3), and (g)  
606    Natural C4 grass (NC4). Color indicates the proportion of a specific PFT in a  $0.5^\circ \times 0.5^\circ$  grid.

607

608    **Figure S2.** Heat plots showing the relationship between predicted and satellite-derived SOS. SOS  
609    data was randomly sampled (10%) from each PFT in the Northern Hemisphere and was excluded  
610    from the calibration of spring phenology models. a–p1: predictions were generated using six spring  
611    phenology models at the PFT scale. Diagonal lines are 1:1 lines, indicating perfect agreement  
612    between predicted and satellite-derived SOS. Colors indicate the percentage of pixels within each  
613    bin.

614

615    **Figure S3.** Spatial pattern of averaged SOS during the period 1982–2012 at the PFT scale. a–d was  
616    SOS inferred from satellite observations and h–p1 shows the SOS predicted by five phenology  
617    models. Pie charts beneath each model indicate the differences between predicted and  
618    satellite-derived SOS; a positive value indicates that the model produced later spring onset than  
619    observed, and vice versa.

620

621    **Figure S4.** Maps of RMSE (days) between satellite-derived SOS and model simulations at the PFT  
622    scale. Results are based on six spring phenology models: (a–g) Spring Warming, (h–n) Sequential,

623 (o–u) Parallel, (v–b1) UniChill, (c1–i1) Unified, and (j1–p1) DORMPHOT. Colors indicate  
624 differences between satellite- and model-derived SOS.

625

626 **Figure S5.** Changes in satellite-derived and model-predicted SOS at the PFT scale during the period  
627 1982–2012. Figures S5a–g show linear trends estimated from satellite-derived SOS, and Figures  
628 S5h–w1 show results based on six spring phenology models: (h–n) Spring Warming model, (o–u)  
629 Sequential model, (v–b1) Parallel model, (c1–i1) UniChill model, (j1–p1) Unified model, and  
630 (q1–w1) DORMPHOT model.

631

632 **Figure S6.** Variation of satellite-derived and model predicted SOS over the period 1982-2012. a-f  
633 shows the results across the temperate broadleaved evergreen (TeBE) based on six spring phenology  
634 models while g-l indicates the results across temperate broadleaved deciduous (TeBD).

635

636 **Figure S7.** Comparison between individual phenology extraction method and their ensemble mean  
637 over the period 1982-2012. Bars and error bars indicate the temporal average and standard deviation  
638 of SOS for each PFT, respectively.

639 **Figure legends**

640 **Figure 1.** Heat plots showing the relationship between predicted and satellite-derived SOS. SOS data  
641 was randomly sampled (90%) from each PFT in the Northern Hemisphere and was applied to the  
642 calibration of spring phenology models. Figure 1a–p1: predictions were generated using six spring  
643 phenology models at the PFT scale. Diagonal lines are 1:1 lines, indicating perfect agreement  
644 between predicted and satellite-derived SOS. Colors indicate the percentage of pixels in each bin  
645 area.

646

647 **Figure 2.** Spatial pattern of averaged SOS in the period of 1982–2012. (a) satellite-derived SOS, (b)  
648 SOS predicted by the Spring Warming model, (c) Sequential model, (d) Parallel model, (e) Unichill  
649 model, (f) Unified model, and (g) DORMPHOT model. The subplot in the bottom left of each spring  
650 phenology model shows the relationship between satellite-derived SOS and model prediction  
651 (\*denotes significant correlation at  $P < 0.05$ ). Figure 2e and i show the distribution of SOS across the  
652 latitude gradient (30°N–75°N).

653

654 **Figure 3.** Boxplots of root mean square error (RMSE, days) between satellite-derived SOS and  
655 model-simulated SOS (from 1982 to 2012) across seven main PFTs in the Northern Hemisphere.

656

657 **Figure 4.** Maps of RMSE (days) between satellite-derived SOS and model simulations. RMSEs were  
658 determined at the pixel scale during the period 1982–2012. Figures 4a–f show the spatial distribution  
659 of RMSEs across the Northern Hemisphere based on six spring phenology models including the (a)  
660 Spring Warming model, (b) Sequential model, (c) Parallel model, (d) UniChill model, (e) Unified

661 model, and (f) DORMPHOT model. Figure 4g is the probability of RMSEs across the Northern  
662 Hemisphere, with vertical lines showing the median of RMSEs.

663

664 **Figure 5.** Changes in satellite-derived and model-predicted SOS during the period from 1982 to 2012.  
665 Figures 5a and b–g indicate linear SOS trends inferred from satellite observation and model  
666 simulations, respectively. Dotted regions indicate that the trends were significant at  $P < 0.05$ .

667

668 **Figure 6.** Linear trends of satellite-derived SOS and model simulations at the PFT scale. \*indicates  
669 that detected trends were statistically significant at  $P < 0.05$ .

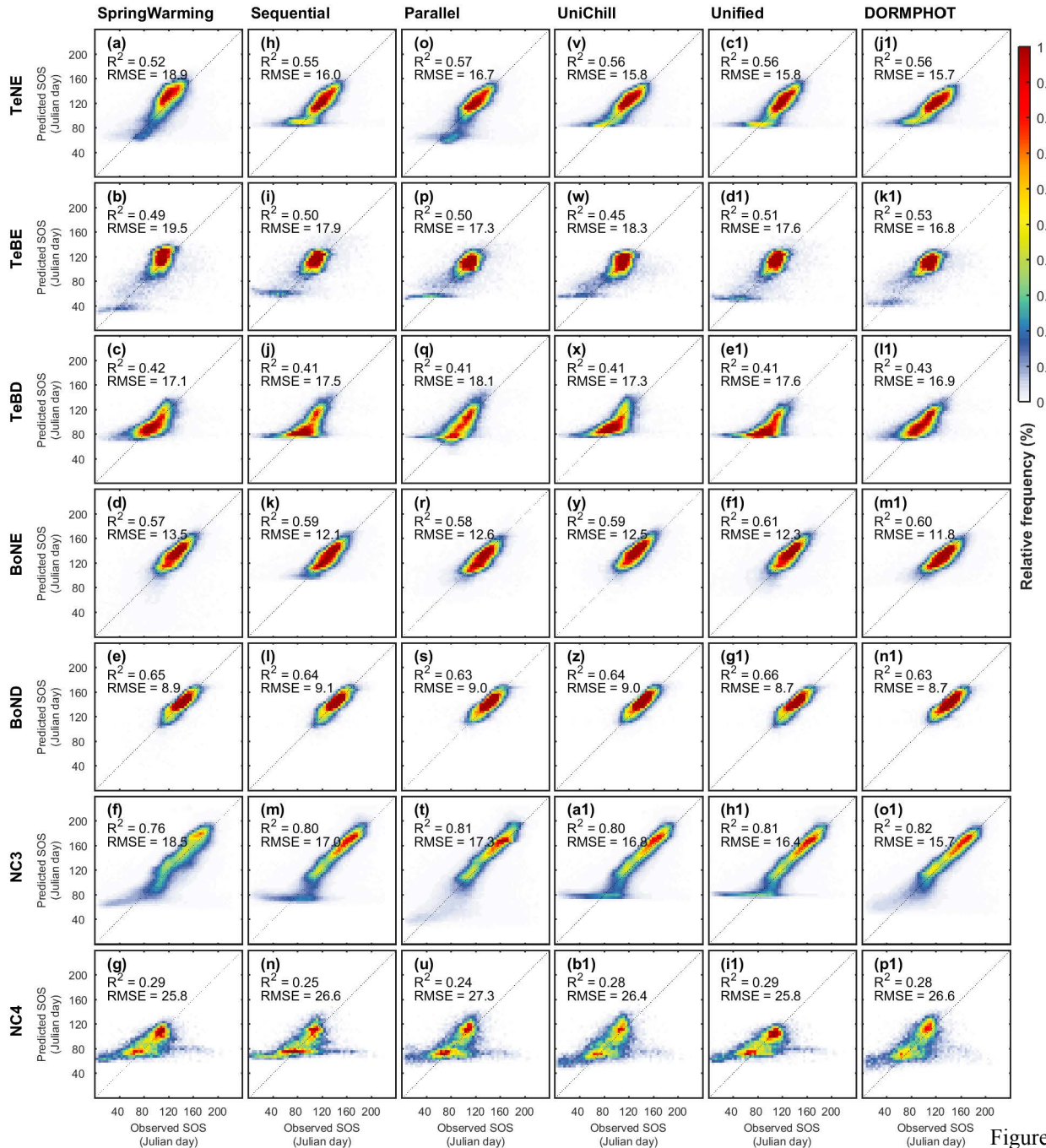
**Table 1.** Estimates of six spring phenology models for each PFT and their performance.

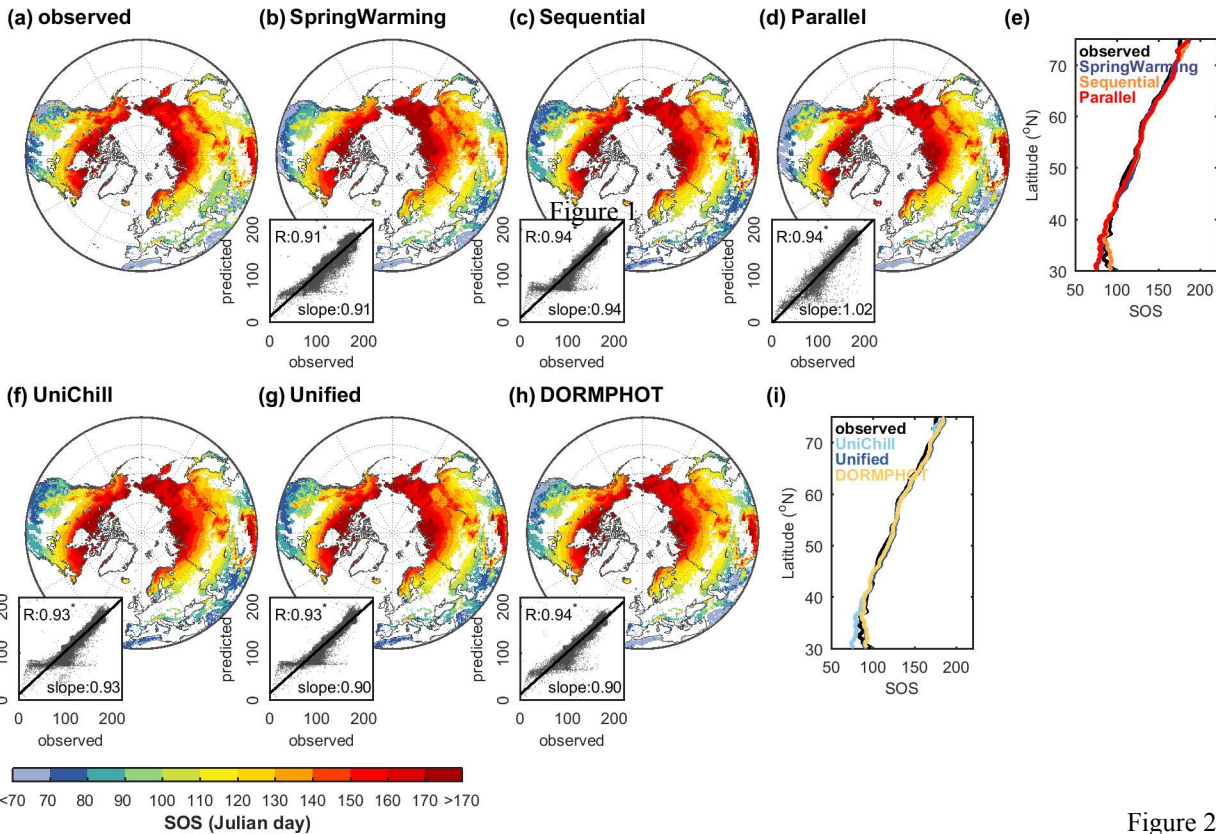
Models		Model Parameters										Model Evaluation <sub>Internal</sub>			
PFTs		alpha	beta	Fcrit	Af	-	-	-	-	-	-	-	RMSE	R <sup>2</sup>	AIC
a. Spring Warning	TeNE	-0.07	15.00	498.24	19.69	-	-	-	-	-	-	-	18.9	0.52*	1.24E + 0
	TeBE	-0.16	8.54	498.86	25.52	-	-	-	-	-	-	-	19.5	0.49*	1.68E + 0
	TeBD	-0.05	12.64	270.24	8.30	-	-	-	-	-	-	-	17.1	0.42*	4.03E + 0
	BoNE	-0.59	6.29	226.33	40.00	-	-	-	-	-	-	-	13.5	0.57*	1.22E + 0
	BoND	-0.65	3.60	381.57	39.99	-	-	-	-	-	-	-	8.9	0.65*	3.65E + 0
	NC3	-0.08	0.95	359.88	8.54	-	-	-	-	-	-	-	18.5	0.76*	3.58E + 0
	NC4	-0.05	32.77	495.09	30.73	-	-	-	-	-	-	-	25.8	0.29*	8.97E + 0
PFTs		alpha	beta	Ccrit	Fcrit	Tb	Td	Ta	Tc	Af	-	-	RMSE	R <sup>2</sup>	AIC
b. Sequential	TeNE	-0.20	-5.31	179.60	63.90	7.04	1.24	-99.38	76.63	7.31	-	-	16.0	0.55*	1.17E + 0
	TeBE	-0.35	-12.76	144.92	66.42	0.27	0.78	-99.21	83.74	36.41	-	-	17.9	0.50*	1.63E + 0
	TeBD	-0.14	-6.35	170.32	353.07	5.07	1.86	-57.10	92.72	42.81	-	-	17.5	0.41*	4.06E + 0
	BoNE	-0.14	1.84	180.57	497.71	-4.86	0.72	-81.55	98.63	37.53	-	-	12.1	0.59*	1.17E + 0
	BoND	-0.40	53.11	55.21	384.22	-7.79	2.39	-58.06	-0.94	33.08	-	-	9.1	0.64*	3.67E + 0
	NC3	-0.18	-4.46	150.49	462.42	-1.55	1.26	-63.99	90.50	38.49	-	-	17.0	0.80*	3.47E + 0
	NC4	-0.05	27.59	170.58	62.61	9.77	5.68	-29.41	89.49	20.31	-	-	26.6	0.25*	9.05E + 0
PFTs		alpha	beta	Ccrit	Fcrit	Tb	Td	Ta	Tc	Af	Kmin	-	RMSE	R <sup>2</sup>	AIC
c. Parallel	TeNE	-0.03	-6.94	145.13	243.68	-17.61	1.13	-59.44	4.13	26.34	0.09	-	16.7	0.57*	1.19E + 0
	TeBE	-0.10	14.59	118.10	226.64	-5.54	1.78	-73.80	0.03	11.99	0.11	-	17.3	0.50*	1.61E + 0
	TeBD	-0.65	-0.19	112.23	229.55	-12.06	4.01	-61.37	4.76	14.88	0.08	-	18.1	0.41*	4.11E + 0
	BoNE	-0.02	-11.11	139.52	154.15	-15.62	1.99	-55.54	4.33	26.99	0.05	-	12.6	0.58*	1.18E + 0
	BoND	-0.13	34.52	163.59	171.01	-8.93	0.95	-99.54	3.28	11.09	0.01	-	9.0	0.63*	3.68E + 0
	NC3	-0.02	-8.90	192.43	78.55	-9.13	3.97	-89.87	5.54	11.98	0.08	-	17.3	0.81*	3.48E + 0
	NC4	-0.11	-17.57	173.36	263.35	-10.94	0.83	-30.64	27.76	26.96	0.01	-	27.3	0.24*	9.12E + 0

PFTs	alpha	beta	Tb	Ta	Tc	Ccrit	Fcrit	-	-	-	-	<b>RMSE</b>	<b>R<sup>2</sup></b>	<b>AIC</b>	
d. UniChill	TeNE	-0.18	3.95	0.00	0.00	4.41	88.05	19.47	-	-	-	16.2	0.56*	1.18	
	TeBE	-0.11	11.31	0.00	0.00	-2.67	68.74	16.26	-	-	-	18.3	0.45*	1.64	
	TeBD	-0.08	2.26	0.01	0.00	2.45	58.94	42.52	-	-	-	17.3	0.41*	4.05	
	BoNE	-0.38	4.60	0.66	0.02	-3.95	39.25	13.78	-	-	-	12.5	0.59*	1.14	
	BoND	-0.97	0.24	0.39	0.01	-11.53	39.77	20.09	-	-	-	9.0	0.64*	3.60	
	NC3	-0.39	1.86	0.01	0.00	7.50	82.99	22.29	-	-	-	16.8	0.80*	3.46	
e. Unified	NC4	-0.08	9.22	0.00	0.00	0.82	29.07	52.29	-	-	-	26.4	0.28*	9.02	
	PFTs	alpha	beta	Tb	Ta	Tc	w	z	Ccrit	deltaP	-	-	<b>RMSE</b>	<b>R<sup>2</sup></b>	<b>AIC</b>
	TeNE	-0.38	6.43	0.00	0.00	-1.93	759.34	-0.05	93.11	41	-	-	15.8	0.56*	1.17
	TeBE	-0.31	9.36	0.01	0.00	7.30	605.88	-0.06	74.56	189	-	-	17.6	0.51*	1.62
	TeBD	-0.21	5.70	0.01	0.00	4.43	235.74	-0.03	86.62	105	-	-	17.6	0.41*	4.07
	BoNE	-0.39	7.87	0.01	0.00	0.45	210.11	-0.05	80.85	22	-	-	12.3	0.61*	1.18
f. DORMPHOT	BoND	-0.35	6.76	0.77	0.02	-3.52	1379.60	-0.07	77.56	129	-	-	8.7	0.66*	3.59
	NC3	-0.37	4.05	0.01	0.00	-1.99	494.70	-0.04	85.39	195	-	-	16.4	0.81*	3.43
	NC4	-0.03	2.77	0.03	0.00	4.63	110.80	-0.01	0.65	62	-	-	25.8	0.29*	8.96
	PFTs	DLCrit	Dcrit	Ccrit	Fcrit	aD	bD	aC	cC	dF	gT	hDL	<b>RMSE</b>	<b>R<sup>2</sup></b>	<b>AIC</b>
	TeNE	12.75	29.43	99.68	19.45	0.05	23.17	0.01	18.41	-0.30	0.33	0.05	15.7	0.56*	1.16
	TeBE	11.01	31.94	24.38	16.32	0.04	20.42	0.02	14.59	-0.76	0.25	0.11	16.8	0.53*	1.60
f. DORMPHOT	TeBD	10.47	28.42	12.49	14.88	0.03	13.36	0.01	16.13	-0.90	0.30	0.02	16.9	0.43*	4.01
	BoNE	9.69	31.21	63.20	15.81	0.91	4.91	0.01	9.70	-0.59	0.25	0.15	11.8	0.60*	1.15
	BoND	10.63	55.42	61.95	19.70	0.44	16.78	0.02	-11.01	-0.44	13.26	14.34	8.7	0.63*	3.45
	NC3	10.42	21.38	8.65	21.99	0.02	6.79	0.01	15.72	-0.77	0.30	0.04	15.7	0.82*	3.38
	NC4	10.58	33.87	49.70	6.03	0.94	19.39	0.41	0.92	-0.05	14.34	11.66	26.6	0.28*	9.04

Note: R<sup>2</sup> represents the percentage of variance explained by the model (\*P < 0.01). AIC: Akaike Information

Criterion; the lowest AIC indicates the optimum model for the simulation of spring phenology. NSE: Nash–Sutcliffe efficiency index; higher (positive, ranging from 0 to 1) NSE values indicate higher model reliability.





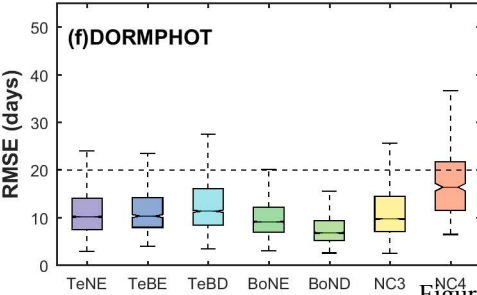
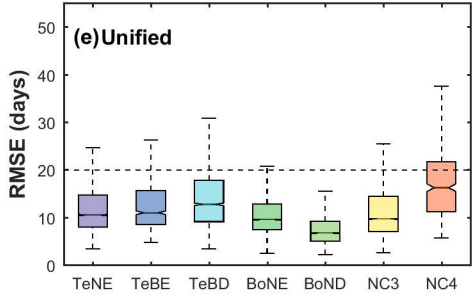
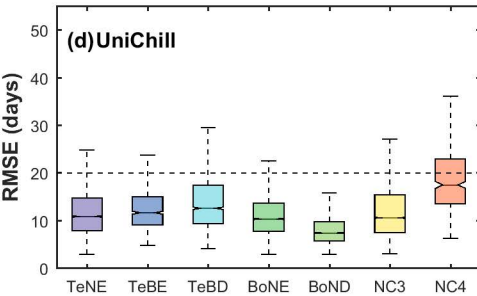
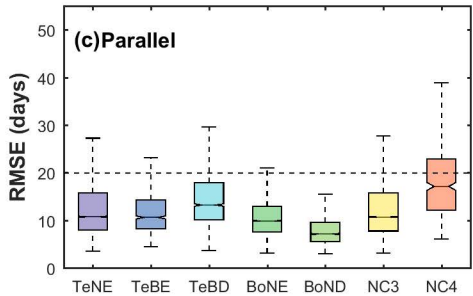
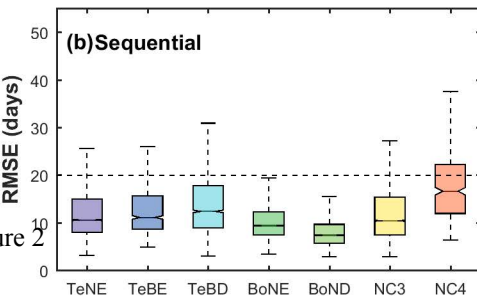
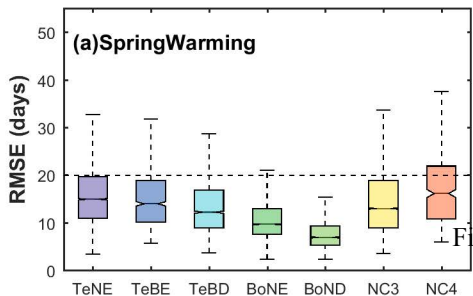


Figure 2

Figure 3

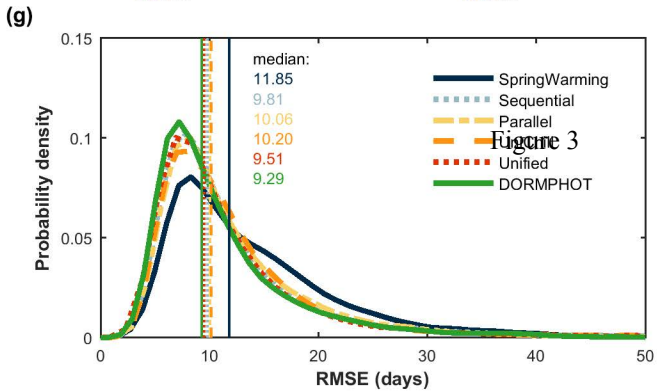
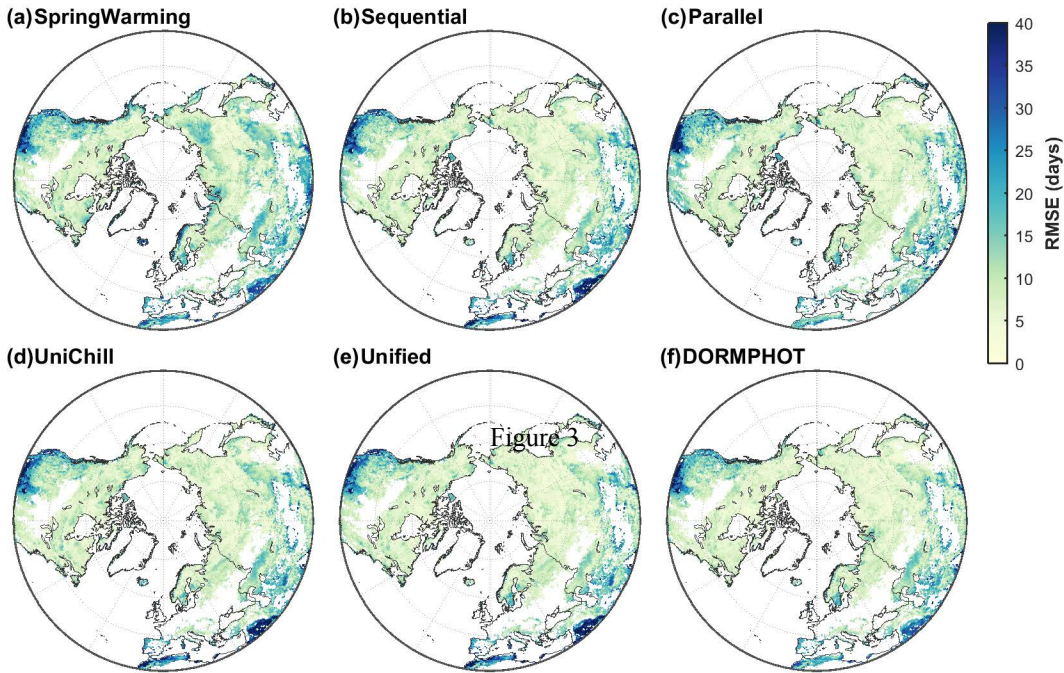
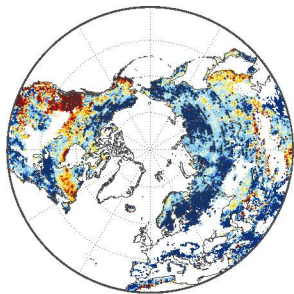
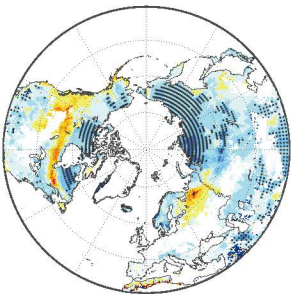


Figure 4

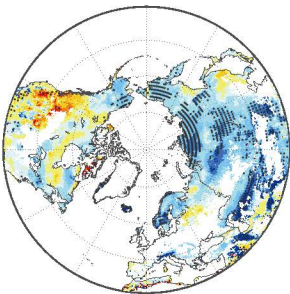
**(a) observed**



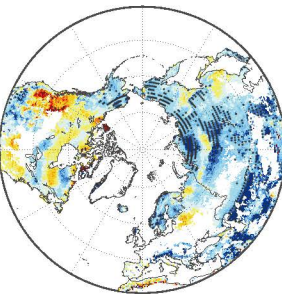
**(b) SpringWarming**



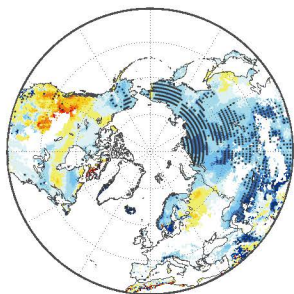
**(c) Sequential**



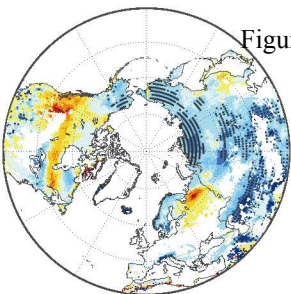
**(d) Parallel**



**(e) UniChill**



**(f) Unified**



**(g) DORMPHOT**

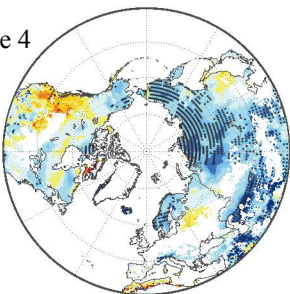


Figure 4

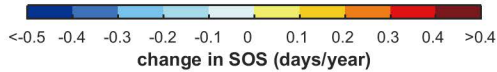


Figure 5

Figure 6

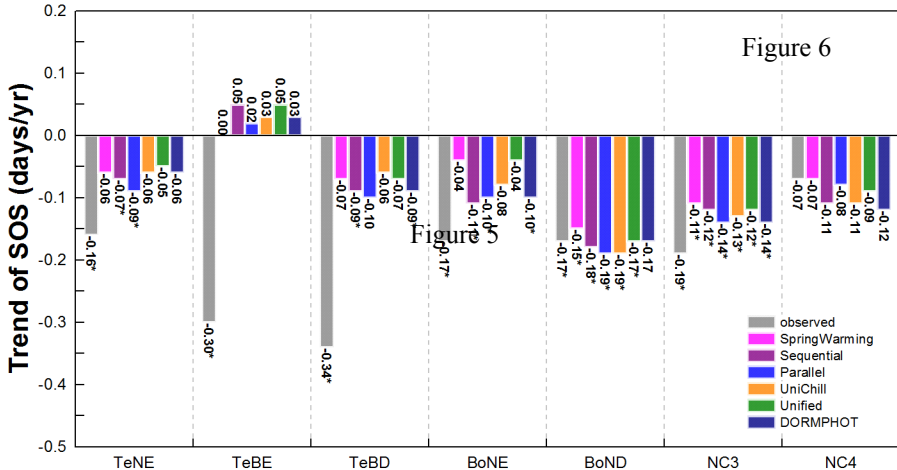
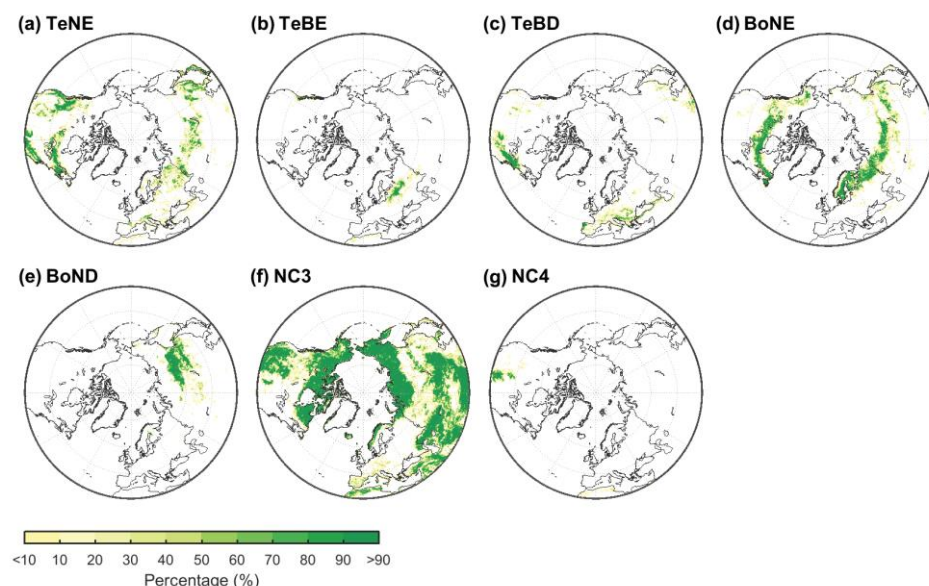
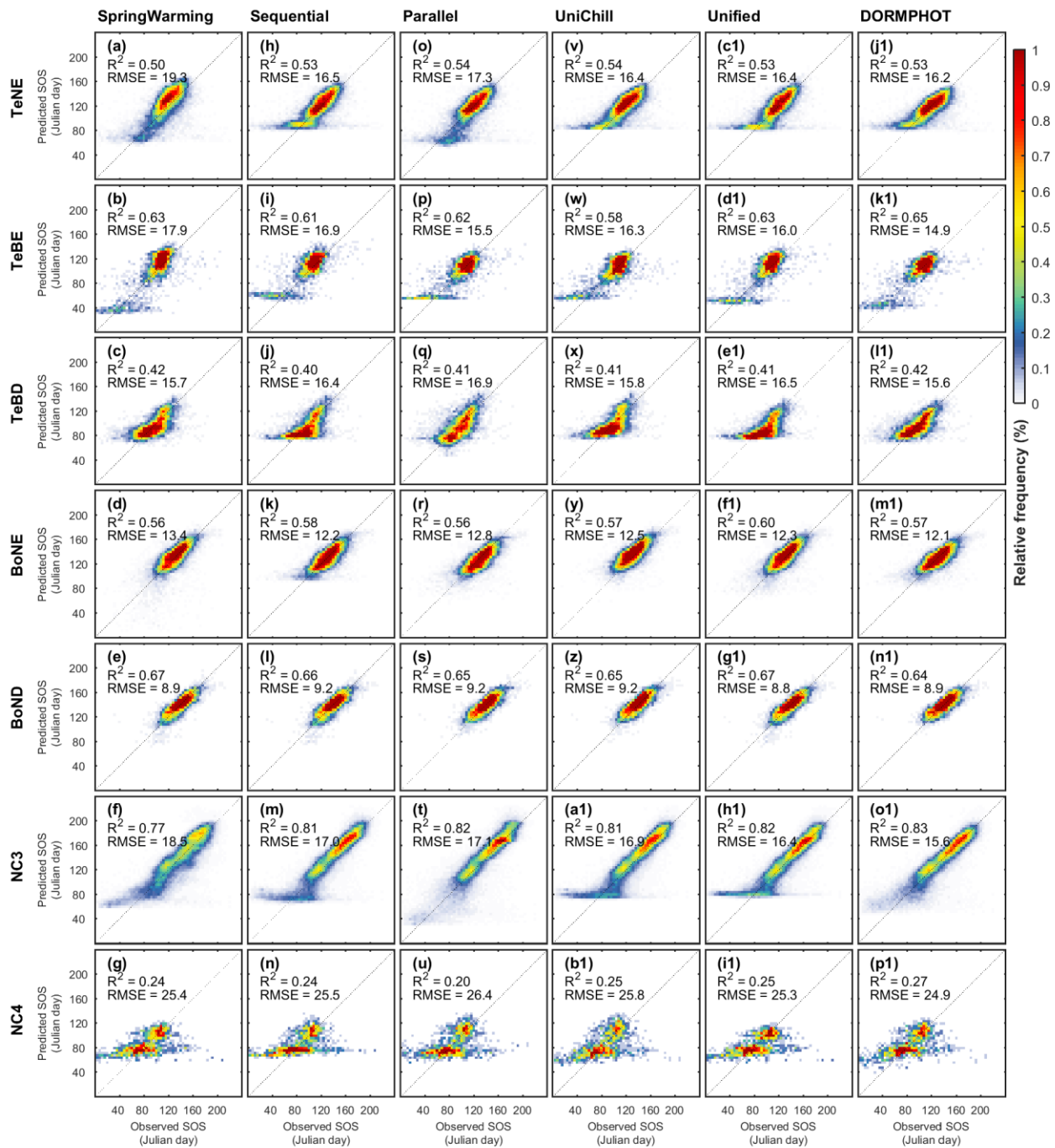


Figure 6  
Figure 9.17\*

**Figure S1.** Spatial distribution of the fractional cover of PFTs across the Northern Hemisphere ( $> 30^\circ \text{N}$ ). Seven main PFTs were included: (a) Temperate needleleaf evergreen (TeNE), (b) Temperate broadleaved evergreen (TeBE), (c) Temperate broadleaved deciduous (TeBD), (d) Boreal needleleaf evergreen (BoNE), (e) Boreal needleleaf deciduous (BoND), (f) Natural C3 grass (NC3), and (g) Natural C4 grass (NC4). Color indicates the proportion of a specific PFT in a  $0.5^\circ \times 0.5^\circ$  grid.



**Figure S2.** Heat plots showing the relationship between predicted and satellite-derived SOS. SOS data was randomly sampled (10%) from each PFT in the Northern Hemisphere and was excluded from the calibration of spring phenology models. a–p1: predictions were generated using six spring phenology models at the PFT scale. Diagonal lines are 1:1 lines, indicating perfect agreement between predicted and satellite-derived SOS. Colors indicate the percentage of pixels within each bin.



**Figure S3.** Spatial pattern of averaged SOS during the period 1982–2012 at the PFT scale. a–d was SOS inferred from satellite observations and h–p1 shows the SOS predicted by five phenology models. Pie charts beneath each model indicate the differences between predicted and satellite-derived SOS; a positive value indicates that the model produced later spring onset than observed, and vice versa.

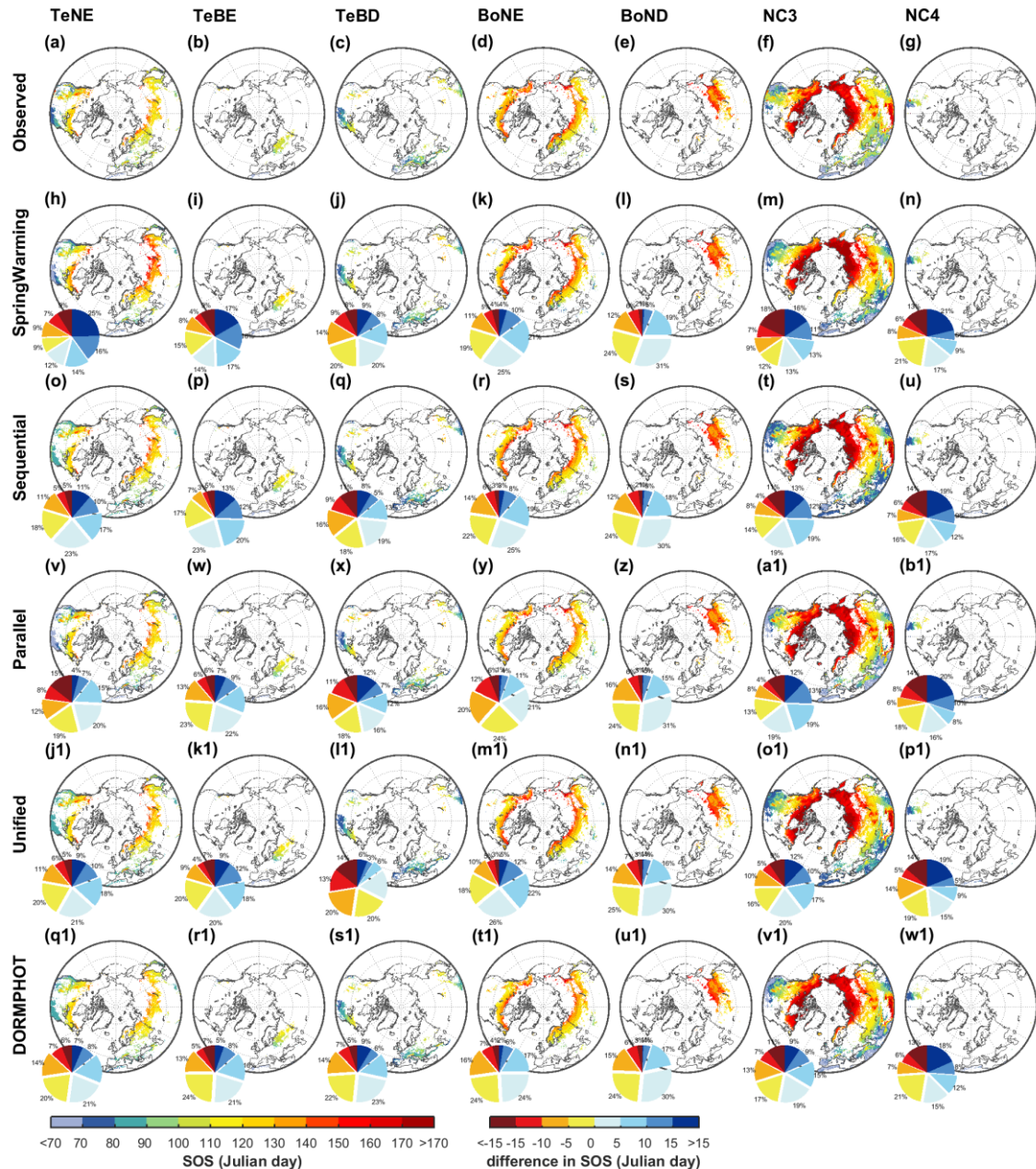


**Figure S4.** Maps of RMSE (days) between satellite-derived SOS and model simulations at the PFT scale. Results are based on six spring phenology models: (a–g) Spring Warming, (h–n) Sequential, (o–u) Parallel, (v–b1) UniChill, (c1–i1) Unified, and (j1–p1) DORMPHOT. Colors indicate differences between satellite- and model-derived SOS.

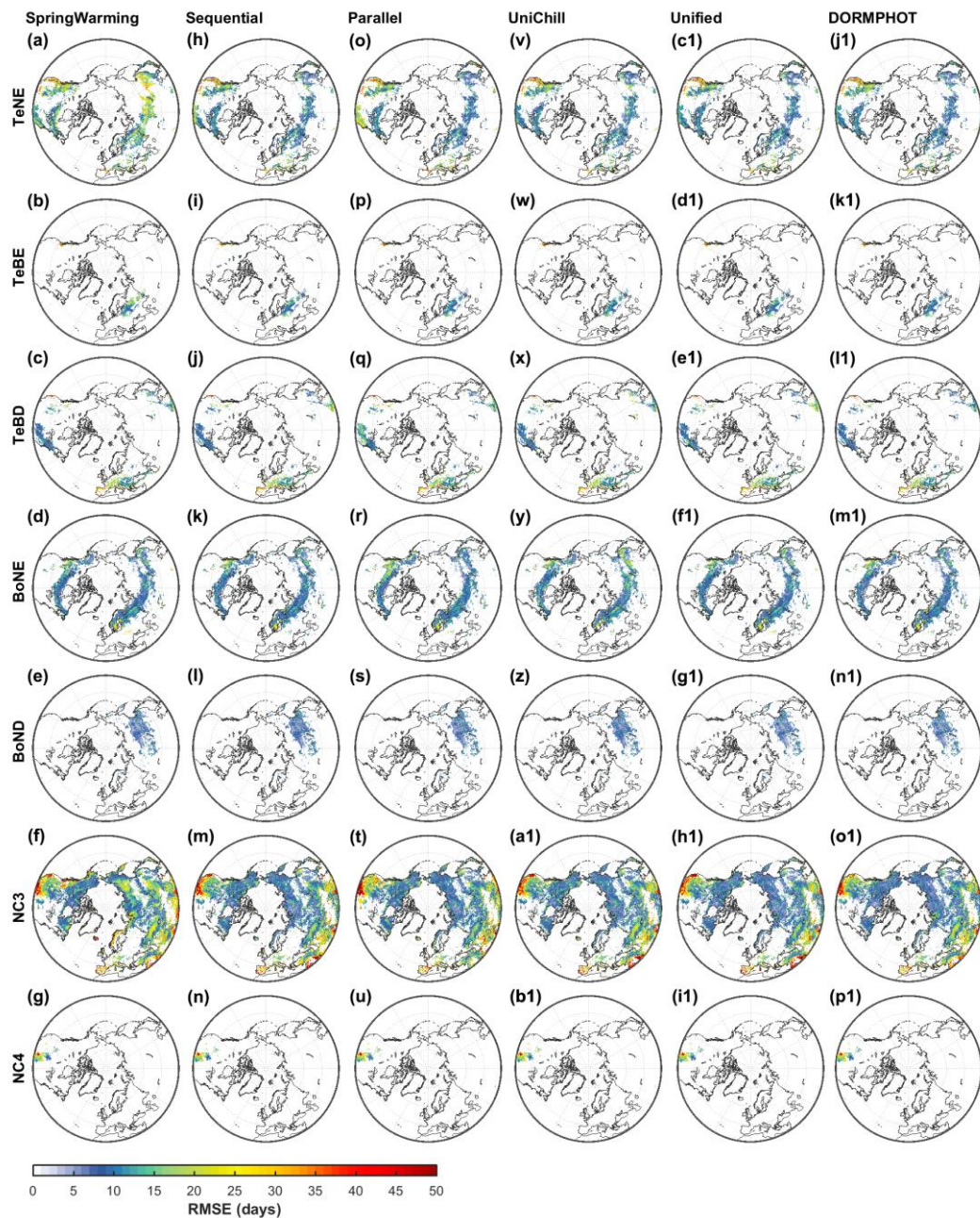


**Figure S5.** Changes in satellite-derived and model-predicted SOS at the PFT scale during the period 1982–2012. Figures S5a–g show linear trends estimated from satellite-derived SOS, and Figures S5h–w1 show results based on six spring phenology models: (h–n) Spring Warming model, (o–u) Sequential model, (v–b1) Parallel model, (c1–i1) UniChill model, (j1–p1) Unified model, and (q1–w1) DORMPHOT model.

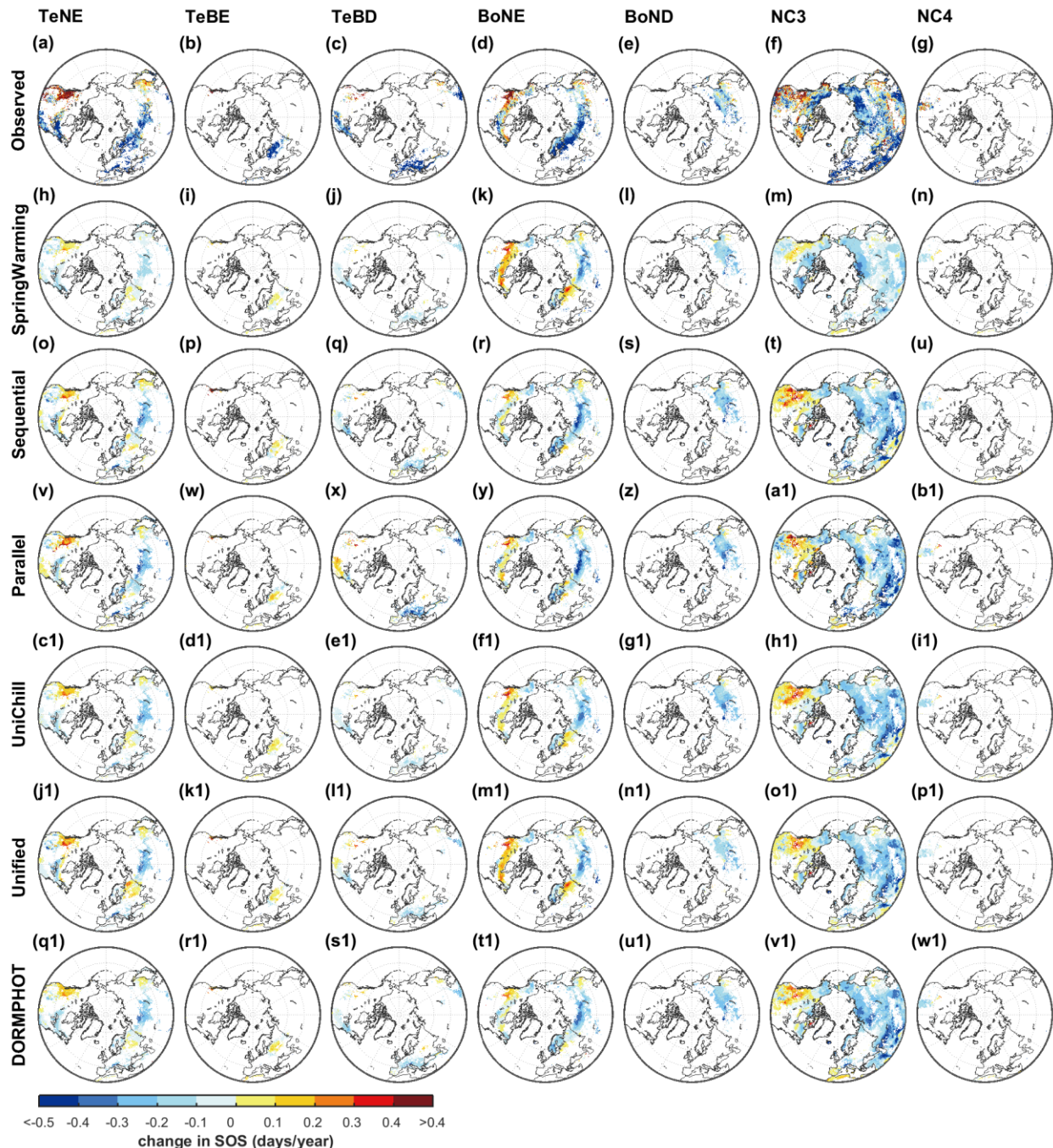


**Figure S6.** Variation of satellite-derived and model predicted SOS over the period 1982-2012. a-f shows the results across the temperate broadleaved evergreen (TeBE) based on six spring phenology models while g-l indicates the results across temperate broadleaved deciduous (TeBD).

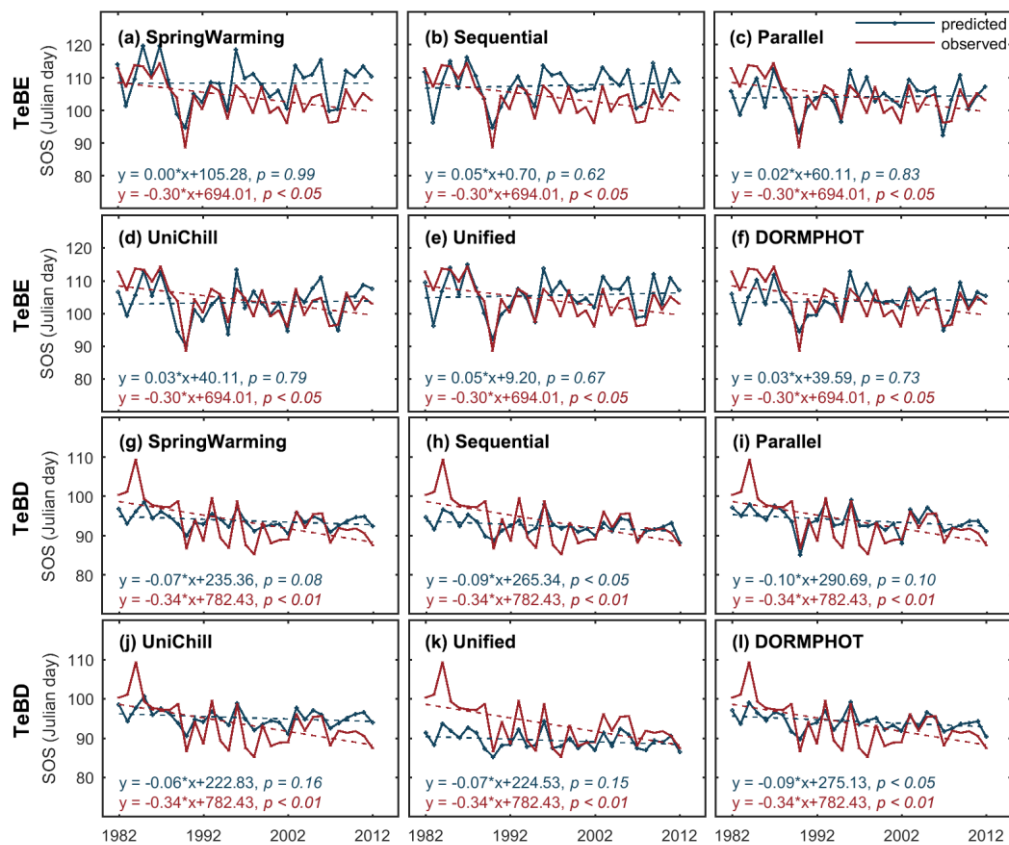


**Figure S7.** Comparison between individual phenology extraction method and their ensemble mean over the period 1982-2012. Bars and error bars indicate the temporal average and standard deviation of SOS for each PFT, respectively.

